DOE Final Technical Report
DE-FG02-01ER63226

Summary

Non-targeted (bystander) effects of ionizing radiation are caused by intercellular signaling; they include production of DNA damage and alterations in cell fate (i.e. apoptosis, differentiation, senescence or proliferation). Biophysical models capable of quantifying these effects may improve cancer risk estimation at radiation doses below the epidemiological detection threshold. Understanding the spatial patterns of bystander responses is important, because it provides estimates of how many bystander cells are affected per irradiated cell. In a first approach to modeling of bystander spatial effects in a three-dimensional artificial tissue, we assumed the following: (1) The bystander phenomenon results from signaling molecules (S) that rapidly propagate from irradiated cells and decrease in concentration (exponentially in the case of planar symmetry) as distance increases. (2) These signals can convert cells to a long-lived epigenetically activated state, e.g. a state of oxidative stress; cells in this state are more prone to DNA damage and behavior alterations than normal and therefore exhibit an increased response (R) for many end points (e.g. apoptosis, differentiation, micronucleation). These assumptions were implemented by a mathematical formalism and computational algorithms. The model adequately described data on bystander responses in the 3D system using a small number of adjustable parameters.

Mathematical models of radiation carcinogenesis are important for understanding mechanisms and for interpreting or extrapolating risk. There are two classes of such models: (1) long-term formalisms that track pre-malignant cell numbers throughout an entire lifetime but treat initial radiation dose-response simplistically and (2) short-term formalisms that provide a detailed initial dose-response even for complicated radiation protocols, but address its modulation during the subsequent cancer latency period only indirectly. We argue that integrating short- and long-term models is needed. As an example of this novel approach, we integrated a stochastic short-term initiation/inactivation/repopulation model with a deterministic two-stage long-term model. Within this new formalism, the following assumptions are implemented: radiation initiates, promotes, or kills pre-malignant cells; a pre-malignant cell generates a clone, which, if it survives, quickly reaches a size limitation; the clone subsequently grows more slowly and can eventually generate a malignant cell; the carcinogenic potential of pre-malignant cells decreases with age.

The effectiveness of high-LET radiation per unit dose increases as dose rate decreases. This “inverse dose rate effect” is seen in radon-induced lung carcinogenesis. We suggest a biologically-motivated mechanism based on radiation-induced direct and bystander-effect-related risks: During radon exposure, only a fraction of cells are traversed by alpha particles. These irradiated cells have an increased probability of being initiated into a pre-malignant state. They release signals, which convert some nearby unirradiated cells to an activated state. When already pre-malignant cells are activated, their proliferation (promotion) rate increases. If a radiation dose is sufficient to activate most susceptible cells, protracting the exposure does not substantially decrease the number of activated cells, but prolongs the activated state during which pre-malignant cell proliferation is accelerated. This mechanism is implemented in a low-dose-rate extension of our carcinogenesis model, which integrates both short- and long-term modeling approaches, and was applied to radiotherapy-induced second cancer risk estimation. Model predictions adequately describe the data on radon-induced lung carcinogenesis in humans and rats, using few adjustable parameters. Conclusions about the relative importance of promotion vs. initiation for radon carcinogenesis are similar to those reported with the two-stage clonal expansion model, but a mechanistic explanation for promotion is provided.

I. *Biophysical Models of Radiation Bystander Effects: Spatial Effects in Three-Dimensional Tissues*

Summary

Non-targeted (bystander) effects of ionizing radiation are caused by intercellular signaling; they include production of DNA damage and alterations in cell fate (i.e. apoptosis, differentiation, senescence or proliferation). Biophysical models capable of quantifying these effects may improve cancer risk estimation at radiation doses below the epidemiological detection threshold. Understanding the spatial patterns of bystander responses is important, because it provides estimates of how many bystander cells are affected per irradiated cell. In a first approach to modeling of bystander spatial effects in a three-dimensional artificial tissue, we assumed the following: (1) The bystander phenomenon results from signaling molecules (S) that rapidly propagate from irradiated cells and decrease in concentration (exponentially in the case of planar symmetry) as distance increases. (2) These signals can convert cells to a long-lived epigenetically activated state, e.g. a state of oxidative stress; cells in this state are more prone to DNA damage and behavior alterations than normal and therefore exhibit an increased response (R) for many end points (e.g. apoptosis, differentiation, micronucleation). These assumptions were implemented by a mathematical formalism and computational algorithms. The model adequately described data on bystander responses in the 3D system using a small number of adjustable parameters.

There is considerable evidence that ionizing radiation affects cells that are located near the site of irradiation but are not themselves traversed by any particle or photon tracks. Such non-targeted radiation effects are diverse and cell type specific. They include increased mutagenesis and genomic instability, differentiation, micronucleus formation, and either decreased or increased response as regards plating efficiency, apoptosis or proliferation. These phenomena, which have been termed radiation-induced bystander effects, were observed not only in cell culture but also *in vivo*.

Due to the discovery of bystander effects, it is becoming clear that cells making up an organism respond to ionizing radiation collectively, as parts of large interconnected groups, in addition to individually. Radiation-induced damage to any cell within a group will generate signals that affect many other group members. These bystander signals can induce DNA damage in cells that have not themselves been irradiated and can alter their behavior by perturbing the dynamic equilibrium between becoming committed to proliferation, apoptosis, quiescence or differentiation. The molecular identities of the signals have not yet been determined, but it is known that propagation of bystander signals from cell to cell can involve diffusion through the extracellular medium, migration of molecules directly between cells through gap junctions, or both.

The net consequence of bystander phenomena for a multicellular organism may be either amplification or suppression of radiation-induced damage to the organism, because mechanisms favoring both types of responses can be activated by intercellular signaling. Which mechanisms dominate appears to be highly dependent on the cell type and experimental conditions. For example, in situations where bystander signals induce predominantly differentiation and apoptosis, thereby removing many potentially damaged cells from the clonogenic pool, a net anti-carcinogenic effect may occur. Conversely, if bystander-induced mutagenesis is prevalent, a pro-carcinogenic outcome is expected.

The main goal of the present paper is to translate the currently available conceptual understanding of the bystander effect, such as the role of oxidative stress as a likely mediator for this effect, into a quantitative mathematical model. Our model focuses specifically on the spatial patterns of the bystander effect. Although describing the details of biochemical signaling pathways is beyond the scope of this model, the formalism is intended to be as mechanistic as possible without undue complexity.

The data set of Belyakov *et al.* for bystander responses in an artificial human three-dimensional skin system is modeled. In this experiment, only a thin plane of cells was irradiated with an α-particle microbeam, and bystander effect end points (apoptosis and micronucleus yield) were measured in parallel planes located at various distances from the irradiated one. This particular data set was selected because it provides rather detailed information on spatial propagation of the bystander response. In addition, it measures the bystander effect in a tissue surrogate instead of in a monolayer culture and therefore may be a better approximation of processes occurring *in vivo*.

Quantitative modeling of the spatial aspect of bystander effects is particularly relevant in situations where most cells have only a small probability of suffering any "hits"—as would be the case at low radiation doses and/or low dose rates and/or high LET. Under such conditions, it is important to predict how many bystander cells (i.e. what volume of tissue) will be affected per each cell directly "hit" by an ionizing track. The model developed here can provide such estimates and thus may have important implications for radiation protection, radiotherapy and understanding radiation-induced carcinogenesis at low doses/dose rates.

MODEL HYPOTHESES AND THEIR MATHEMATICAL IMPLEMENTATION

Based on current data, we propose a plausible sequence of events involved in the bystander effect. Implementing this scenario mathematically involves the following eight specific assumptions and derivation steps:

1. Molecules Involved in the Bystander Effect

The bystander effect is produced by radiation-induced signals (referred to here as S) that travel from irradiated cells to their neighbors and, by molecular mediators, that are induced by these signals in target cells. Recent studies of bystander effects and patterns of cell signaling in general suggest that the intercellular signals (S) can be proteins (e.g. cytokines such as TGF-β), small messengers (e.g. cAMP, ATP, IP3), or oxidants such as reactive oxygen and nitrogen species (ROS and RNS). They are released into the medium by irradiated cells and can act in an autocrine, paracrine or long-range endocrine manner, depending on the context and on cell properties (e.g. receptor number on a cell surface). The smallest molecules (those that are <1 kDa in molecular weight) can also migrate directly between neighboring cells through gap junctions.

The net effect of bystander signals on unirradiated cells appears to be rather persistent induced overproduction of ROS and RNS. These oxidant molecules are known to play a regulatory role in many biochemical pathways by redox signaling. Specifically, they have been implicated in radiation-induced bystander effects and genomic instability and in other "non-classical" radiobiological phenomena that are observed in some cell lines [i.e. low-dose hypersensitivity/induced radioresistance and the death-inducing effect].

Signal-induced overproduction of oxidants leads to accelerated accumulation of DNA damage and alterations in cell fate, which are the experimentally measured bystander responses (here called R). In general, a moderate elevation in oxidant concentration induces cells to undergo more rapid turnover (i.e., differentiation and apoptosis of some and compensatory proliferation of others) and migration. Progressively higher oxidant levels cause mutagenesis, cell senescence, and necrosis. All of these outcomes are observed as forms of the bystander effect, depending on the cell type and irradiation conditions.

2. Cell Activation

The bystander signal (or group of signals) S acts in a probabilistic binary manner by causing cells to switch from an undisturbed background state (no excess oxidant production, low rate of DNA damage accumulation) to an activated bystander effect state (increased oxidant production, elevated rate of DNA damage accumulation). This assumption is based on experimental results suggesting that excess damage in bystander cells is approximately independent of dose over a broad range of radiation doses, i.e. "on or off" in quality.

At any time t after irradiation, a bystander cell located at distance x from the irradiation site will have a probability of being in the activated state rather than in the background state. This probability, which we denote by P_a, is described by the following differential equation:

$$dP_a/dt = c_2S(1 - P_a) - c_3P_a. \qquad (1)$$

Here c_2 and c_3 are rate constants for transition between the two states: c_2 determines the rate at which the activated state is induced, and c_3 determines the rate of the opposite process, where activated cells revert back to background. The term c_2S represents our assumption that the probability per unit time of converting a cell from the background state to the activated state is proportional to the concentration of the bystander signal (S) at the given time and location. The term $1 - P_a$ indicates the probability that the given cell has not yet undergone this transition and is therefore available for being activated by the bystander signal. Finally, the term $-c_3P_a$ indicates that the activated state tends to spontaneously revert to background at a fixed probability per unit time.

3. Spatial Propagation of Bystander Signals

Propagation of S in space (i.e. from cell to cell) and induction of the activated state by S occur rapidly, on the scale of a few minutes to a few hours. For example, measurement of production of DNA double-strand breaks in bystander fibroblasts by visualizing γ-H2AX complex formation showed that new complexes are being formed as soon as 2–10 min after irradiation in cells as distant as 5–7.5 mm away from irradiated ones. These data suggest that the processes of S propagation and P_a induction proceed at a speed of >8 μm/s. Other studies found that supra-background γ-H2AX complexes began to appear in bystander cells somewhat more slowly, 30 min to a few hours after irradiation.

4. Accumulation of DNA Damage in Bystander Cells

Once bystander cells have been activated, they accumulate DNA damage at an abnormally high rate, until they revert to the background state. The return to background (which can be called deactivation) happens relatively slowly, on the scale of many hours to days—much more slowly than initial activation.

These conclusions are supported by measurements of various DNA damage-related end points (e.g. γ-H2AX foci, fractions of apoptotic and micronucleated cells) in the bystander effect context, which indicates that these end points typically do not return to background levels for several days. A similar temporal pattern is observed in directly irradiated cells, where these same damage markers remain elevated for days to weeks after exposure to radiation, particularly to high-LET α particles. Other phenomena, which may share some common causes with bystander effects, e.g. genomic instability in multiple generations of cultured descendants of irradiated cells and persistence of an inflammatory state in animal organs irradiated *in vivo*, have an even longer duration.

These observations are consistent with measurements of ROS levels in irradiated cell cultures, which also show that a return to baseline oxidant concentration occurs only many days to weeks after irradiation. It is likely that elevated ROS levels are sustained by a positive feedback loop, where oxidants stimulate their own production, e.g. by damaging mitochondria and inducing genes like *COX2*, whose products act in ROS-generating pathways.

Our interpretation of these findings is that DNA damage accumulates more rapidly than normal as long as the activated state (i.e. a state of oxidative stress) is maintained. Although opposing processes (such as DNA repair and removal of dead cells) also operate continually, damage levels cannot return completely to

background for at least as long as the cells remain activated and DNA continues to be attacked at an elevated rate.

5. Temporal Patterns of the Bystander Effect

The data cited to support assumptions 3 and 4 imply that the processes of bystander signaling (i.e. induction of cells into the activated state) and bystander response (i.e. persistence of cells in the activated state before reversion to the background state) can be thought to operate on different time scales.

After an acute radiation exposure, directly hit cells emit the signal S, which quickly propagates outward to bystander cells and begins to activate them. Soon it reaches its maximal spatial range. Most bystander cells that are located within the range of S propagation (and are susceptible to being activated) will be converted to the activated state, and those outside this range will remain mostly unaffected.

The time necessary for these processes to occur, which we call T, is, as previously cited experiments suggest, no more than a few minutes or hours long. In contrast, the typical time needed for bystander cells to revert to the background state, i.e. $1/c_3$, where c_3 is as defined in Eq. (1), is much longer—many hours to several weeks. These differences in time scale between signal propagation/cell activation and persistence of the activated state indicate that in Eq. (1), the term representing the first set of processes, i.e. $c_2S(1 - P_a)$, is numerically much larger than the term representing the second process, c_3P_a. Therefore, the smaller term c_3P_a can be neglected, and Eq. 1 can be reduced to the following:

$$dP_a/dt = c_2S(1 - P_a). \qquad (2)$$

This approximate formulation reflects the intuitive conclusion that if the damage-inducing activated state is long-lasting, brief delays in its inception caused by kinetics of S propagation/cell activation can be disregarded, as if all activated cells were activated simultaneously.

Equation (2) can be solved to yield the following expression for P_a:

$$P_a = 1 - \exp\left[c_2 \int_0^T S(t)\, dt\right]. \qquad (3)$$

This approximation holds as long as $T \ll 1/c_3$, as experimental data suggest. It shows that P_a does not depend on S directly, but is affected only by the time integral of S [i.e. $\int_0^T S(t)\, dt$], and thus this time integral is what determines the maximal spatial range of S.

6. Mechanism of Bystander Signal Propagation

To generate an explicit solution for P_a, the mathematical form of the time integral of S [i.e. $\int_0^T S(t)\, dt$] needs to be specified. We assume this integral to be an exponentially decreasing function of distance in the case of interest here, where the system effectively has planar symmetry, so that analyzing the gradient involves equations in just one fixed spatial direction (x).

This exponential function is intended to represent spatial kinetics observed in juxtacrine or paracrine signal relay systems, for example calcium wave propagation. While we do not propose that calcium waves are responsible for the bystander effect, the modes of cell-to-cell signaling operating in calcium wave and bystander processes are probably similar. There appears to be some justification for making this mechanistic analogy, because signal propagation velocities identified by studies of physical injury-induced calcium waves and radiation-induced bystander effects are quite consistent—approximately 10 μm/s. In addition, calcium fluxes were directly observed in the bystander experiment context in cells exposed to conditioned medium from irradiated cells.

In many tissue types, stimulation of one or several cells by agents such as physical injury produces a non-regenerative signaling wave that spreads outward by the “fire-diffuse-fire” mechanism to neighboring cells,

decreasing in amplitude over time and distance: A stimulated cell “fires”, releasing the signal, the signal diffuses locally to reach the adjacent cell through the extracellular medium or through gap junctions, and the adjacent cell responds by “firing” its own burst of signal.

Perhaps the simplest way of describing this type of process mathematically is to assume that each time the signal passes from an activated cell to its immediate neighbor, its intensity is reduced by a constant fraction F. In cases of planar symmetry, the signal intensity (Fs) reaching a cell located i cell diameters away from the initial source of the stimulus is therefore $Fs = (1 - F)^i$. If the attenuation factor F is >0, a finite number of cells will be affected (i.e. the signal will have a finite spatial range). If F approaches 0, the range will approach infinity. For a signal source in the (y, z) plane (i.e. the plane $x = 0$), this simple function can be rewritten to accommodate distances in micrometers rather than cell diameters: $Fs = \exp(-c_1 x)$, where x is distance in micrometers, the adjustable parameter $c_1 = -\ln(1 - F)/d$, and d is the average cell diameter in micrometers.

By combining this expression with our previous assumptions, the following equation for the spatial dependence of the time integral of S is produced:

$$\int_0^\infty S(t)\,dt = Nf(D)\exp(-c_1 x). \qquad (4)$$

Here N is the number of irradiated cells located in the plane $x = 0$ that are capable of producing S. The function $f(D)$ represents the dependence of S on radiation dose/dose rate (D). So far there are insufficient data to specify the shape of this functional dependence, which may, for example, be linear or saturating. For the purposes of this paper, where a data set based on a single-dose acute exposure is used, we treat the function $f(D)$ as a constant. Finally, the parameter c_1, as defined previously, represents the logarithmic rate at which the time integral of S decreases with distance.

7. Approximate Explicit Solution for Probability of Cell Activation

By substituting Eq. (4) into Eq. (3), an explicit solution approximating the probability (P_a) that a bystander cell at distance x away from the irradiated plane will be induced into the activated state can be generated:

$$P_a = 1 - \exp[-c_2 N f(D) \exp(-c_1 x)]. \qquad (5)$$

8. Complete Mathematical Form of the Model

According to our assumptions, while a bystander cell is in the activated state, it accumulates DNA damage at an abnormally high rate. However, the rate of damage production is not the only determinant of observed damage yield that is reported in experimental studies. There are multiple other concurrent processes (e.g. damage repair, cell cycle progression, elimination of apoptotic cells from the tissue). These processes interact with damage production, for example by removing damage (e.g. repair of DNA double-strand breaks) or, alternatively, making the damage observable (e.g. onset of apoptosis after cell cycle checkpoints are reached). Consequently, each type of damage (e.g. γ-H2AX foci, apoptosis, micronucleation, DNA hypomethylation) has its own temporal kinetics in activated bystander cells *(53)*.

In addition, it is likely that there is a sensitive subpopulation of cells (which we call the susceptible population) in which the bystander response is induced at greater likelihood than in other cells exposed to the same amount of signal *(31)*. This assumption is supported by findings of multiple experiments, where only a few percent of cells exhibit bystander effect end points even at high radiation doses [e.g. *(6, 9)*]. The actual properties that make cells within this group susceptible to the bystander signal (perhaps position in the cell cycle) are not fully understood and do not affect the structure of our model.

These factors of heterogeneous susceptibility to bystander effects and damage-specific temporal kinetics are beyond the scope of our model, which is concerned primarily with the spatial patterns of bystander responses. We account for the effects of these factors indirectly by assuming that the probability (R_n) that a bystander cell will exhibit a particular damage end point (n) at the time of experimental observation (*Tobs*)

is proportional to the probability that this cell had previously been activated (P_a). Using Eq. (5) for P_a, this assumption is represented mathematically as follows:

$$R_n = K_n(1 - \exp[-c_2 Nf(D) \exp(-c_1 x)]). \quad (6)$$

Here K_n is a damage end point-specific and observation time-specific proportionality constant.

Equation (6) is consistent with the intuitive conclusion that at the time of observation (*Tobs*), the spatial region where the maximum incidence of the damage of interest (e.g. apoptosis, micronucleation) is found is the same region where the maximum fraction of cells were induced into the activated state by bystander signals.

PARAMETER ESTIMATION

Equation (6) contains three parameters: c_1, $c_2Nf(D)$, and K_n. The current level of knowledge about bystander phenomena does not make it feasible to specify the exact nature of bystander signals and the activation process and therefore provide reliable bounds on these parameters from sources independent of the modeled data set. Consequently, parameter values were adjusted to fit the data of Belyakov *et al.*.

The parameter c_1, which represents the decay rate of the time integral of S with distance away from irradiated cells, can vary over a very wide biologically plausible range, depending on the molecular nature of the signal, cell type and extracellular environment. For example, soluble ligands for the epidermal growth factor receptor (EGFR), which are produced after injury and irradiation, have a mean travel range of <5 to tens of micrometers depending on receptor number and rate of endocytosis. Injury-induced intercellular calcium waves are not observed at all in some cell types, but in others they propagate over tens to hundreds of micrometers, or even over much larger distances. Bystander effect studies reveal a similar variability in signal range. *In vitro* experiments involving confluent cell monolayers covered by a liquid medium suggest essentially infinite propagation distances, where the signal reached the edges of the culture dish hundreds to thousands of micrometers away from the irradiation site in times as short as 10 min. However, measurements of bystander effect propagation in three-dimensional tissue-like systems, such as the data set of Belyakov *et al.* used here, show a finite spatial range of several hundred micrometers. A larger finite range of several millimeters was found in some *in vivo* studies involving partial-body irradiation of mice. Because of this variability, and because the identity of the bystander signals is not specified in the model, we allowed c_1 to be freely adjusted to the data.

The combination $c_2Nf(D)$ also plays an important role in the spatial dependence of the bystander response. The number of cells directly hit by radiation (N) could be estimated from the experiment of Belyakov *et al.*: It was equal to 400–800 cells per 8-mm length of the irradiated plane. We chose the mid-range estimate of 600 cells/8 mm, or 75 cells/mm. All of these cells were assumed to produce S. The dose/dose-rate-dependent function $f(D)$, however, cannot be determined from this data set, which involves only a single acute irradiation of 10 α particles/cell over ~2 min. Because the value of $f(D)$ is absorbed into the value of the product $c_2Nf(D)$, for convenience we assigned it to 1.0 concentration × h. The remaining constant c_2, with units of (concentration × h)$^{-1}$, was allowed to be freely adjustable to the data.

The damage/time-specific proportionality constants K_n, where $n = 1$ for apoptosis and 2 for micronucleation, represent the maximum excess fractions of cells expressing these damage end points measured at the observation time *Tobs* = 72 h. They were adjusted to produce the optimum fit to the data.

In our actual calculations, holding $K_nc_2Nf(D)$ fixed while varying K_n and $c_2Nf(D)$ inversely to each other produced almost no change in the results as long as K_n remained within the range consistent with the data. Consequently, the number of adjustable parameters was, to good approximation, 2 instead of 3.

DATA-FITTING PROCEDURE

The excess (compared with background) fractions of apoptotic and micronucleated cells among bystander cells located at various distances away from the irradiated plane were determined from Belyakov *et al.*. At each section through the tissue model (starting at 200 μm and continuing until 1100 μm away from irradiated cells, at 100-μm intervals), the background apoptosis or micronucleus yields were subtracted from the corresponding experimental data points. Combined error bars were calculated by taking the square root of the sum of squares of error bars for irradiated and background samples.

Best fits to the resulting apoptosis and micronucleation data sets were produced using the approximate solution for R_n (Eq. 6). Fitting was accomplished by a customized random-restart simulated annealing algorithm written in the FORTRAN programming language, using 10,000 random initial conditions and 10,000 iterations per initial condition. The function that was minimized to obtain a best fit (;th*f*;th) had the following form:

$$f = \sum \left[\frac{W_1(R_1 - A)^2}{dA} + \frac{W_2(R_2 - M)^2}{dM} \right]. \qquad (7)$$

Here A and M are the measured excess apoptotic and micronucleated cell fractions, dA and dM are their error bars, R_1 and R_2 are the approximate solutions given by Eq. (6) using corresponding constants K_1 and K_2, W_1 and W_2 are the respective weights for the two types of data, and the summation is over all experimental tissue sections from 200 to 1100 μm away from the irradiated plane. The weight coefficients were defined as

$$W_1 = \frac{1}{\sum \frac{A}{dA}}, \qquad W_2 = \frac{1}{\sum \frac{M}{dM}}. \qquad (8)$$

Fitting was performed for the apoptosis data alone (by setting $W_2 = 0$), for the micronucleation data alone (by setting $W_1 = 0$), and for both data sets combined (by keeping W_1 and W_2 as defined).

RESULTS

The best-fit parameter values generated by our algorithm for each of the two data sets and for the combined data are shown in Table 1. Adequate fits were produced in all cases, with the predicted curves intersecting most of the data points/error bars (Figs. 1 and 2).

The best-fit values of parameter c_1 were 0.0208 μm^{-1} for combined data sets, 0.0122 μm^{-1} for the apoptosis data alone, and 0.00648 μm^{-1} for the micronucleation data alone. Thus signal (S) propagation efficiency should decrease by half at a distance of ~30–110 μm and drop to 10% of maximum at ~110–360 μm, depending on the data set. Spatial decay rates of this order of magnitude are reasonable for juxtacrine/paracrine signaling by small molecules. For example, in keratinocytes, the mean distance to which a calcium wave could be propagated was measured at 90–100 μm.

Our model fits the data by generating an almost step-function-like dependence of R_n on distance from the irradiated plane (Figs. 1 and 2). At distances below ~800 μm (using the fit for combined data sets as an example), a plateau region is established where essentially all susceptible cells are activated by the bystander signal (i.e. $P_a \approx 1$). By the time damage is scored (*Tobs* = 72 h), this plateau region exhibits the

maximum yield of excess damage end points (R_n). At greater distances (e.g. 1200–1400 μm), observed excess damage decreases virtually to zero. This putatively occurs because the initial signal S failed to propagate this far away from the irradiated plane and failed to activate the cells present in this more distant region.

From the structure of Eq. (5), it can be deduced that the exponential slope (*Slope*) with which the bystander activation probability P_a decreases at distances beyond the plateau range is linearly dependent on constant c_1. The extent of the plateau range (*Range*) is inversely proportional to c_1 and logarithmically dependent on $c_2Nf(D)$. Mathematical expressions describing the roles of these parameters are:

$$Slope = c_1(1 - P)\ln(1 - P);$$

$$Range = \ln\{c_2Nf(D)/\ln[1/(1 - P)]\}/c_1. \qquad (9)$$

Here P is a chosen threshold value. For example, when P = 0.5, *Range* will represent the depth in tissue at which the activation probability (or excess cell damage) drops by half. This range ($R_{0.5}$) is calculated using best-fit parameters for the combined and separate data sets and is shown in Table 2.

Slope can be more conveniently expressed as the fraction (F) by which the bystander signal is reduced from cell to cell, as defined above. For a typical cell diameter of 10 μm, F is calculated using best-fit parameters for the combined and separate data sets and is also shown in Table 2.

A pictorial representation of model behavior in response to changes in parameter values is shown in Figs. 3 and 4. When only c_1 is varied, with $c_2Nf(D)$ and all other parameters held constant (Fig. 3), the range and slope are both strongly altered. In contrast, when $c_2Nf(D)$ is varied, leaving everything else unchanged (Fig. 4), the slope is unaffected and the range is modified only slightly. To increase the range significantly, $c_2Nf(D)$ needs to be increased dramatically (e.g. 10-fold), because range depends on $c_2Nf(D)$ in a logarithmic manner (Eq. 9). This can be done, for example, by increasing the number of irradiated cells (N) by increasing the thickness of the tissue section exposed to radiation.

As assumed previously (Eq. 6), the bystander response probability R_n is proportional to the activation probability P_a. Consequently, R_n has the same step-function-like spatial pattern as P_a. It is worth noting that whereas the range expression is the same for R_n as for P_a, the slope of R_n depends not only on c_1 but also on K_n. Thus, to obtain the slope for R_n, the *Slope* formula in Eq. (9) needs to be multiplied by K_n.

The quality of the fit of model predictions to the data depends strongly on K_n and *Range* (i.e. $R_{0.5}$). As is evident from Eq. (9), *Range* can remain essentially unchanged as long as $\ln[c_2Nf(D)]$ and c_1 are multiplied by a common factor. Consequently, the fit depends substantially on the ratio of $\ln[c_2Nf(D)]/c_1$ but only weakly on the individual values of these parameters. For example, the best fit for the combined data sets was obtained by $c_2Nf(D) = 2.07 \times 10^8$ (i.e. $\ln[c_2Nf(D)] = 19.2$) and $c_1 = 0.0208$ μm^{-1}, i.e. the ratio of $\ln[c_2Nf(D)]/c_1 = 921$ μm (Table 1). This combination produced $R_{0.5} = 938$ μm (Table 2). Seemingly very different combinations of $c_2Nf(D) = 5.10 \times 10^5$ (i.e. $\ln[c_2Nf(D)] = 13.1$) with $c_1 = 0.0141$ μm^{-1}, and $c_2Nf(D) = 100$ (i.e. $\ln[c_2Nf(D)] = 4.61$) with $c_1 = 0.00520$ μm^{-1}, in fact generated quite similar $\ln[c_2Nf(D)]/c_1$ ratios of 932 and 886 μm, respectively. The values of $R_{0.5}$ produced by these combinations (958 and 956 μm) were also similar to the best-fitting $R_{0.5}$.

Therefore, the data sets analyzed here appear to have sufficient power to estimate the bystander signal range, but they may not be sufficient to specify the individual values of parameters c_1 and $c_2Nf(D)$. For the apoptosis data, the signal range ($R_{0.5}$) is of the order of 950–1000 μm, and for the micronucleation data it is substantially smaller at 650– 700 μm. For the combined data sets, $R_{0.5}$ is apparently dominated by the apoptosis data and is of the order of 930–950 μm. The dominance of the apoptosis data set in the simultaneous fit is not an artifact of the fitting procedure, since both apoptosis and micronucleation data sets were weighted equally, with a correction for the values of the data points. Instead, the large value of

$R_{0.5}$ in the combined fit is driven by the high values of the apoptosis data points at distances 500–800 μm from the irradiated plane.

The substantial difference in signal range between separate fits to apoptosis and micronucleation data may reflect the possibility that apoptosis and micronucleation are induced by different bystander signals. Until the nature of bystander signals is clarified by further research, the simultaneous model fit to both data sets combined may be useful, because the number of adjustable parameters is reduced, and the fit quality is still adequate for all data.

DISCUSSION

We have constructed an analytically solvable, simple quantitative model of the spatial and temporal kinetics of the radiation-induced bystander effect. The main assumptions of this model are based on experimental studies suggesting the existence of at least one (and probably many) rapidly spreading signal, which is produced by irradiated cells and induces long-term alterations of the redox balance (activation) in multiple neighboring cells, leading to accumulation of extra DNA damage and modification of cell behavior. The initial signal itself may be oxidative or non-oxidative in nature.

The model describes the selected data sets adequately, using a limited number of parameters. Only two parameter combinations [c_1 and $c_2Nf(D)$] are required to describe the shape of the bystander response as a function of distance away from the irradiated plane, and the rest act as proportionality constants used for normalization of the data. As new information about the identity of bystander signals and their properties accumulates, increasingly rigorous testing of the model can be performed.

Saturation of the fraction of cells expressing any particular bystander effect end point, which is often observed experimentally, is accounted for by our model. Such saturation could be due to activation of all susceptible cells within the region affected by the bystander signal, followed by expression of the end point by all activated cells. Alternatively, activation may not necessarily lead to expression of the observed end point—a certain probability of expression, which is less than unity, may be involved. In that case, the maximal (saturated) fraction of cells displaying the end point would be the product of three terms: the probability of activation, the susceptible cell fraction, and the probability of expressing the end point after activation of a susceptible cell. Both of these scenarios are consistent with our model.

It is important to note that the model presented here was fitted to a data set generated using an artificial 3D human skin system, which is physiologically much closer to *in vivo* tissues than are commonly used cell cultures. This realism enhances the potential for predicting the spatial ranges of bystander responses in irradiated human organs.

The ability to quantify these responses is particularly important in situations of low-dose/dose-rate and/or high-LET radiation exposure, where not all cells are traversed by ionizing tracks during the exposure period. Direct experimental measurement of risks (e.g. carcinogenesis) associated with such small doses is not feasible, necessitating the use of mathematical models.

The currently accepted method of carcinogenesis risk estimation at low radiation doses—the linear no-threshold (LNT) approach—involves direct linear extrapolation from higher doses. However, bystander effects are likely to provide a significant pro-carcinogenesis contribution at low radiation doses by increasing the cell turnover and mutation rates, thereby potentially enhancing clonal expansion of pre-existing mutant cells and generating new mutant clones. Such conditions may occur, for example, with cancers induced by radon inhalation. The model developed here, which accounts for bystander damage, may enhance current low-dose risk estimation approaches.

II. *A new view of radiation-induced cancer: integrating short- and long-term processes*

Summary

Mathematical models of radiation carcinogenesis are important for understanding mechanisms and for interpreting or extrapolating risk. There are two classes of such models: (1) long-term formalisms that track pre-malignant cell numbers throughout an entire lifetime but treat initial radiation dose-response simplistically and (2) short-term formalisms that provide a detailed initial dose-response even for complicated radiation protocols, but address its modulation during the subsequent cancer latency period only indirectly. We argue that integrating short- and long-term models is needed. As an example of this novel approach, we integrated a stochastic short-term initiation/inactivation/repopulation model with a deterministic two-stage long-term model. Within this new formalism, the following assumptions are implemented: radiation initiates, promotes, or kills pre-malignant cells; a pre-malignant cell generates a clone, which, if it survives, quickly reaches a size limitation; the clone subsequently grows more slowly and can eventually generate a malignant cell; the carcinogenic potential of pre-malignant cells decreases with age.

Introduction

Short- and long-term biologically based models

Biologically motivated mathematical modeling of background and ionizing radiation-induced carcinogenesis has a history spanning more than 50 years. Many of the models can be characterized as short-term, in that they focus on processes occurring during and shortly after. The main advantage of such models is that they provide a detailed initial dose–response relation for short-term endpoints, which are used as surrogates for carcinogenesis. The main disadvantage is that the possibly substantial modulations of the magnitude and shape of this initial dose–response during the lengthy period (multiple years-decades) between irradiation and manifestation of typical solid tumors are not considered mechanistically.

In contrast, another class of biologically motivated models can be characterized as long-term, in the sense that they track carcinogenesis rates throughout the entire life span, e.g., the Armitage-Doll model, the Moolgavkar-Venzon-Knudson two-stage clonal expansion (TSCE) model, and the two-stage logistic model. The main advantage of long-term models is the more detailed treatment of slow carcinogenesis processes, including the modulation of the radiation dose–response during the long latency period. The main disadvantage is that the initial dose–response is typically treated in a non-mechanistic, phenomenological manner.

The need for a new approach: integration of long- and short-term models

The lack of detailed treatment of radiation-specific effects typically limits risk predictions from long-term models to exposure conditions where a simple dose–response relationship holds. Exposures where this relationship is more complex, such as high fractionated radiotherapeutic doses that can lead to treatment-induced cancers in nearby organs are difficult to describe with current long-term models. Conversely, the more detailed dose–responses produced by sophisticated short-term models can be scaled to cancer risks only by considering the effects of factors such as background risks, age at exposure, and time since exposure, which are not explicitly taken into account by the short-term formalisms. A new, unified approach of integrating short- and long-term techniques is needed, where a detailed initial dose–response for pre-malignant cell numbers is produced over a wide range of doses, and changes to the shape of this dose–response during the latency period before the development of cancer are also analyzed in detail. A schematic representation of model unification is provided in Fig. 1.

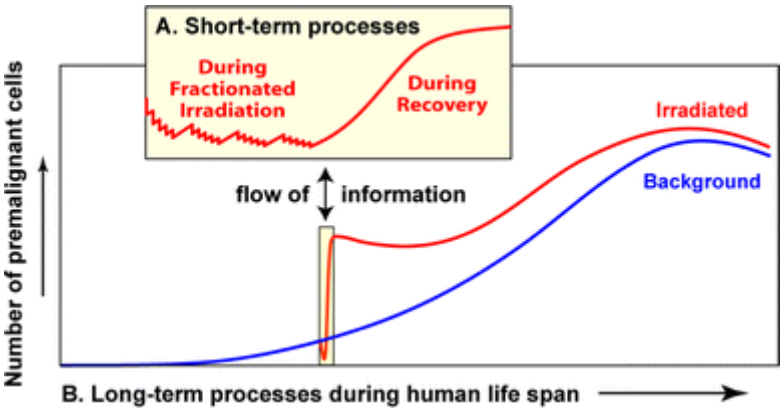

Fig. 1 A general scheme of short- and long-term processes governing the total number of pre-malignant cells. Details are discussed throughout the main text. As the individual ages, the number of viable pre-malignant cells grows, but the curve may turn over and decrease at very old age (*blue line* in the main graph). This pattern parallels background cancer incidence, since cancer risk is assumed to be proportional to the number of pre-malignant cells (discussed in the text). Radiation exposure (e.g., radiotherapy for an existing cancer) initially causes the number of pre-malignant cells to decrease due to cell killing (*red line*). After exposure stops, the irradiated tissues recover, allowing pre-malignant cells to repopulate and reach a number higher than was present before irradiation, i.e., a net excess radiogenic cancer risk is produced. Fluctuations in the number of pre-malignant cells throughout the irradiation and recovery periods (i.e., the short-term processes) are shown in the inset graph

Motivations for the specific unification used here

Here, we provide a specific example of integrating short- and long-term radiation carcinogenesis models. In that a variety of short- and long-term models have been proposed, our approach should be considered as illustrative, intended to investigate the practicality of integrating the two model types. The goal was to produce a novel formalism, which can describe typical patterns of background and radiogenic carcinogenesis with the smallest possible number of adjustable parameters. This goal required multiple simplifying assumptions about the complex multi-step carcinogenesis process. We suggest that for the purposes of generating a preliminary integrated model, the consequent reduction in biological realism is compensated by the reduction in model complexity and number of parameters. More complicated examples of unifying long- and short-term models are certainly possible, e.g., models analyzing multiple pre-malignant cell stages, analyzing genomic instability, and/or analyzing stochastic effects at both time scales, rather than just at short-time scales as we shall do.

Short-term model

The short-term part of our model (Fig. 1a) is the more mathematically intensive part of the integrated formalism. It is based on existing *i*nitiation, *i*nactivation and *r*epopulation (*iir*) models originally designed for analyzing second cancers induced by radiotherapy. This short-term part analyzes normal and pre-malignant stem cells during complex radiation exposure regimens and during the following weeks of tissue recovery. It tracks individual pre-malignant cell clones rather than just the total number of pre-malignant cells. The probability that a pre-malignant clone becomes extinct during radiotherapy can be substantial, so a fully stochastic formalism is used for the population dynamics of pre-malignant cells.

Long-term model

The long-term part of our model (Fig. 1b) approximates carcinogenesis by a process where normal target (e.g., stem) cells can be initiated by spontaneous or radiation-induced mutations to become pre-malignant cells, which can clonally expand and perhaps produce by mutation a fully malignant cell, which then gives rise to cancer after some lag period. The basic assumptions are somewhat similar to those of several long-term models cited above, including the TSCE model. Specifically, our long-term formalism uses the following main assumptions:

- Normal and pre-malignant stem cells are located in specific tissue niches. We here have in mind a general concept of a niche, including, e.g., a clone whose further growth is prevented or slowed by any kind of micro-environmental constraints. The number of niches per organ, and the number of normal or pre-malignant stem cells per niche, is homeostatically regulated. We allow for the possibility that pre-malignant stem cells are regulated somewhat less stringently than their normal counterparts, so that a niche filled with pre-malignant cells can contain more such cells on average than a niche filled with normal cells.
- An initiated stem cell either dies out, or grows into a pre-malignant clone, which quickly (e.g., within a year) fills the entire stem cell niche in which it originated, i.e., "initiates" the whole niche. To expand beyond the first niche, the pre-malignant clone needs to invade an adjacent niche; alternatively, the niche containing the clone can divide into two daughter niches, e.g., colon crypt fission. These processes require years or decades, and may involve acquisition of new mutations.
- Pre-malignant cells in all niches are assumed to gradually lose their carcinogenic potential with age, so that at old age they have a progressively smaller probability of being transformed to malignant cells. This assumption is suggested by a decrease in incidence of most cancers at very old age, e.g., >80 years in humans [Surveillance Epidemiology and End Results (SEER) database, http://seer.cancer.gov] and >800 days in mice. The likely mechanism is senescence of stem cells and/or deterioration of stem cell function, or niche function, with age.
- To reduce the number of model parameters, clonal expansion of pre-malignant stem cell niches is treated deterministically, using a net proliferation rate. In other words, it is estimated by a deterministic "exponential model", instead of the stochastic TSCE model. Given realistic parameter values, the deterministic and stochastic versions of the two-stage model are numerically very similar from birth until old age. In our analyses, by the time irradiation is over and cell repopulation in the exposed organ has occurred, surviving pre-malignant clones have grown to substantial sizes, making extinction very unlikely. This reduces the need for stochastic treatment of clone dynamics during the decades following radiation exposure. At old age, the deterministic approximation predicts an increasing hazard, whereas the stochastic TSCE model predicts a plateau. Considering the evidence cited above about a decrease in cancer incidence at old age, neither behavior is fully realistic. We here instead model the downturn in incidence at old age explicitly, according to the assumption above.

Unification of short- and long-term models

The integration of long- and short-term models will have two features typical of multi-timescale modeling: (1) information is passed in both directions between the two components; and (2) a formally infinite time interval in the short-term model represents a short time interval, here typically several months, in the long-term model (Fig. 1).

The deterministic long-term equations provide the mean number of niches filled with pre-malignant stem cells and the mean number of pre-malignant cells per niche just before irradiation. The stochastic short-term equations then provide the number of these niches that are eradicated by radiation as well as the number of pre-malignant clones that are induced by, and survive, the radiation exposure. Each of these clones is assumed to be independent (i.e., located in a different part of the organ), and to be capable of quickly filling a niche with pre-malignant cells. Therefore, the total number of pre-malignant niches soon after irradiation can be calculated by the stochastic short-term model. The mean of this number is the initial condition for the deterministic long-term equations, which are applied from this point onwards until old age (Fig. 1). Cancer incidence is assumed to be proportional to the total number of pre-malignant cells in all niches, shifted by a lag time. A mathematical description of the model is provided below.

Materials and methods

The mathematical techniques for implementing the assumptions for our specific example of integrating long- and short-term modeling are discussed next. A schematic representation of the concepts is provided in Fig. 2. The notation and interpretations for model parameters are listed in Table 1. Data on both background and radiation-induced cancers are used to estimate the parameters.

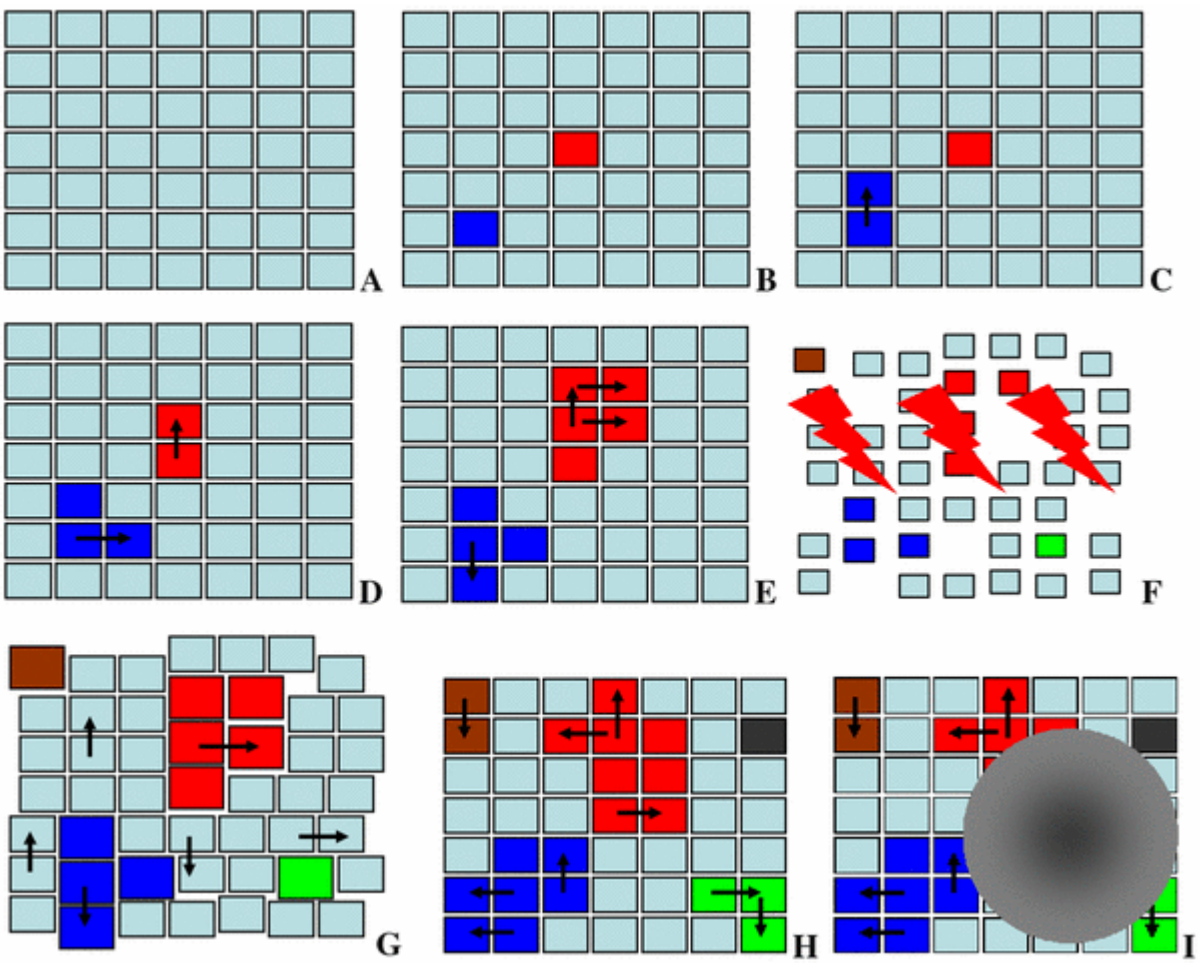

Fig. 2 Schematic representation of proposed pre-malignant cell kinetics. Each *square* represents a tissue niche. *Cyan color* normal cells; *other colors* pre-malignant cells—each *color* indicates a different clone. *Black arrows* invasion of an adjacent niche. The *order of panels* denotes a hypothetical time sequence: a only niches filled with normal cells are present at a young age. b Some niches filled with pre-malignant cells are spontaneously initiated (*red* and *blue*). c–e The pre-malignant clones expand over time by taking over adjacent niches. f Radiation exposure (*lightning symbols*) perturbs the system: some normal and pre-malignant cells are inactivated (niches become smaller), and some niches are completely inactivated (shown by *gaps*). Some new pre-malignant clones are initiated (*green* and *brown*). g After exposure, all niches filled with pre-malignant cells (*red*, *blue*, *green*, *brown*) expand in cell number (undergo promotion, shown by an increase in the size of the squares). Possible promotion of normal niches is neglected. Surviving normal and pre-malignant niches replace the niches inactivated by radiation (shown by *disappearance of the gaps*). h Over many years/decades after irradiation, roughly normal tissue architecture is restored. The promoting effect may disappear, as all niches return to the default size. Meanwhile, replication of existing pre-malignant niches continues (shown by *arrows*), and some new clones appear by spontaneous initiation (shown by the *black square*). i Subsequent mutations in one of the pre-malignant clones produce the first fully malignant cell, which grows into a malignant tumor (*gray mass*)

Table 1 Summary of model parameters

Parameter	Units	Interpretation
a	time^{-2}	Spontaneous stem cell initiation and transformation
b	time^{-1}	Pre-malignant niche replication
c	time^{-2}	Age-dependent pre-malignant cell senescence
δ	time^{-1}	Homeostatic regulation of pre-malignant cell number per niche
Z	cells/niche	Carrying capacity for pre-malignant cells per niche
X	time/dose	Radiation-induced initiation
Y	dose^{-1}	Radiation-induced promotion
α, β	dose^{-1}, dose^{-2}	Stem cell inactivation by radiation
λ	time^{-1}	Maximum net stem cell proliferation (repopulation) rate
L	time	Lag period between the first malignant cell and cancer

Long-term model for background cancers

The long-term model was intended mainly to place the results of the stochastic short-term calculations in an appropriate context, enabling estimation of the effects of age at exposure and time since exposure on predicted cancer risk. Simplicity and parsimony were emphasized. The long-term model in the absence of radiation consists just of a few rather simple deterministic equations, as follows.

Each pre-malignant stem cell in any niche has a certain small probability per unit time (q units = cells^{-1} × time^{-1}) of transforming into a fully malignant cell, and, after a fixed lag time (L), into clinical cancer. These are common assumptions made in many long-term carcinogenesis models, e.g., in the TSCE model. The average number of new fully malignant cells per unit time (A units = time^{-1}) is the product of q and three other variables: the number of stem cell niches filled with pre-malignant cells (M units = niches), the average number of pre-malignant stem cells per niche (ρ units = cells × niche^{-1}), and the probability that the pre-malignant cells remain non-senescent and capable of producing cancer (P). The number of pre-malignant stem cells per niche (ρ) is assumed to be homeostatically regulated (in a qualitatively similar manner to the regulation of normal stem cells), so that it always tends towards a constant number—a carrying capacity Z (units = cells × niche^{-1}). For convenience, the number of pre-malignant stem cells per niche can be redefined as a dimensionless normalized fraction $C = \rho/Z$. The proportionality constant qZ can be removed from the expression for A by defining $N = qZM$ (units = time^{-1}), where N is proportional to the number of pre-malignant niches. Consequently, A can be written in the following simplified form:

$$A = NCP \tag{1}$$

Equation (1) is an approximation for the incidence hazard function: it gives the mean expected number of new malignant cells (i.e., eventual cancers) per individual per year, whereas the hazard (H) given in (2) is the yearly probability that a malignant cell occurs in a previously healthy individual at age t:

$$H = A / \left(1 - \int_0^t A\,du\right) \tag{2}$$

The functions A and H are numerically very similar for realistic parameter values; they diverge substantially only if cancer incidence is high. We use the exact hazard H for data fitting in the companion paper, but use the simpler expression for A in the equations below, keeping in mind its interpretation and limitations.

The function N is described by the following differential equation (3), where t is patient age, the constant a (units = time^{-2}) is proportional to the spontaneous stem cell initiation rate, and the constant b (units = time^{-1}) is the pre-malignant niche replication rate:

$$dN/dt = a + bN \quad (3)$$

Equation (3) can be adjusted to accommodate an assumption that more than one mutation is needed to initiate a stem cell by replacing the constant a with the composite term $at^{\kappa-1}$, where κ is the necessary number of mutations. However, doing so does not substantially improve the fit of the model to the data sets analyzed, and so was not used as the default because it introduces an extra adjustable parameter κ. The results for fitting multi-stage extensions of our model (i.e., where $\kappa > 1$) to SEER data for female breast and male lung cancers are shown in Fig. 3.

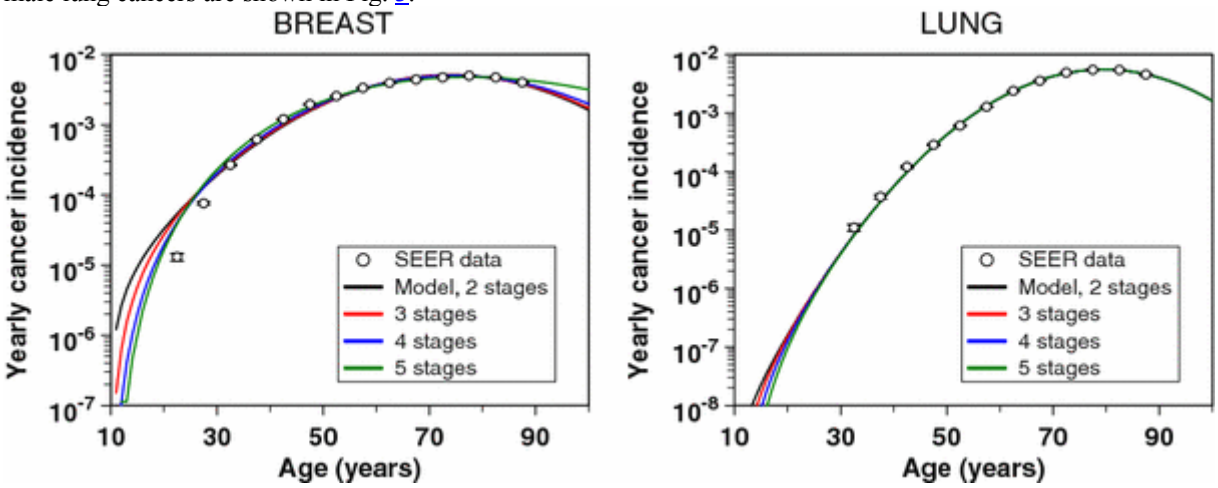

Fig. 3 Fits of the long-term part of our model to spontaneous incidence data for female breast and male lung cancers from SEER (the data for young ages were excluded because cancer incidence in these age groups is likely to be dominated by genetic predisposition). *Error bars* represent 95% confidence intervals. The different curves represent our default two-stage formalism and its multi-stage extensions described in the main text. These extended versions of the formalism do not alter the fit substantially

---

The function C is regulated by the following logistic differential equation, where δ (units = time^{-1}) is a rate constant representing the strength of homeostatic control of the number of pre-malignant cells per niche:

$$dC/dt = \delta C(1 - C) \quad (4)$$

For background carcinogenesis the solution $C = 1$ is used.

The probability that the pre-malignant cells remain non-senescent and capable of producing cancer (P) is described by a Gaussian function with an adjustable parameter c (units = time^{-2}), which cannot become negative even as age approaches infinity, contrary to the expression used by others:

$$P = \exp\left[-ct^2\right] \quad (5)$$

For convenience later, when radiation-induced excess relative risk (ERR) will be calculated, it is useful to express patient age (t) as the sum of age at exposure (T_x) and time since exposure (T_y). The background cancer risk function without radiation ($A_{bac}(T_x, T_y)$) follows from (1) and (3–5), assuming that no pre-malignant cells are present at birth (i.e., that $N(0) = 0$):

$$A_{bac}(T_x, T_y) = (a/b)\left(\exp\left[b(T_x + T_y)\right] - 1\right)\exp\left[-c(T_x + T_y)^2\right] \quad (6)$$

Here, the duration of radiation exposure is ignored, because it is considered to be short compared with the multi-year time scale of the long-term carcinogenesis processes.

Effects of radiation

Short-term processes

The exposure scenario analyzed here is radiotherapy for an existing malignancy, where there are K daily dose-fractions, all of equal size d in some nearby organ, with treatment gaps during the weekends.

Straightforward generalizations to variable doses per fraction, to other temporal patterns, and/or to cases where one must consider dose-volume histograms are omitted for brevity. A single acute dose exposure is a simple special case, where the number of fractions is $K = 1$.

The short-term part of the model considers *i*nitiation, *i*nactivation, and *r*epopulation (*iir*) of normal and pre-malignant stem cells during the radiation regimen and a recovery period of about a month (Fig. 1). Niche takeover by pre-malignant cells that survive the irradiation and modulation of niche size by radiogenic promotion (discussed below) are here also considered short-term processes. They are assumed to be essentially completed by a few months following exposure, before the long-term processes of spontaneous initiation and niche replication, which operate on the time scale of multiple years, start to have an appreciable effect (Fig. 1).

Normal stem cells are treated deterministically because their number per organ is assumed to be large. In contrast, the number of pre-malignant stem cells per clone is much smaller, and extinction of some pre-malignant clones is a real possibility. Consequently, a stochastic approach described below is used to estimate the average number of live pre-malignant niches when post-irradiation long-term processes begin.

For simplicity, both normal and pre-malignant stem cells are assumed to be equally radiosensitive. The cell surviving fraction (S) is described by the standard linear-quadratic (LQ) function with parameters α and β for dose-fractions of size d:

$$S = \exp\left[-\alpha d - \beta d^2\right] \tag{7}$$

The normal stem cell number (n) in the entire organ just before the kth dose-fraction is denoted by $n^-(k)$, and the number just after the kth dose-fraction by $n^+(k)$. The reduction in n due to initiation of a few normal stem cells is neglected. Inactivation is calculated as follows:

$$n^+(k) = S n^-(k) \tag{8}$$

Repopulation of normal stem cells during radiotherapy is assumed to be regulated by homeostatic mechanisms—if some stem cells are killed by radiation, surviving stem cells are induced to proliferate with the goal of restoring the total number of normal stem cells in the organ (n) to the number present before irradiation (ν). It should be noted that ν is conceptually and numerically distinct from the carrying capacity Z introduced above for pre-malignant stem cells per pre-malignant niche. The homeostatic regulation of cell proliferation during the time gaps between dose-fractions and after the last fraction is described by the Logistic differential equation, where λ (with units = time^{-1}) is the maximum net proliferation rate:

$$dn/dt = \lambda n\left[1 - n/\nu\right] \tag{9}$$

Equations (7–9) allow the calculation of the normal stem cell number $n(t)$ in the entire organ at all relevant times t throughout the radiation exposure and recovery periods. Explicit results for $n(t)$ are provided in the Appendix.

We assume that the long-term growth advantage of pre-malignant cells manifests itself only on the scale of years and decades, and is negligible on the much shorter time scale of a few weeks of radiotherapy. Consequently, the maximum net proliferation rates for normal and pre-malignant stem cells are assumed to be equal, described by the parameter λ.

As discussed above, radiation initiates some normal stem cells, making them pre-malignant. The number of cells initiated in the kth dose-fraction is assumed to be Poisson distributed, with average $aXI(k)$, where X is an adjustable parameter (units = time × dose^{-1}) and the function $I(k)$ (units = dose) is given by:

$$I(k) = d S n^-(k)/\nu = dn^+(k)/\nu \tag{10}$$

Our assumptions allow the birth, death, and initiation rates for normal stem cells calculated deterministically by (7–10) to be used as parameters for a stochastic formalism for pre-malignant cell clones. Each such clone is initiated as a single cell in some random niche by the kth dose-fraction, and can fluctuate in cell number during subsequent radiotherapy due to the opposing effects of inactivation and repopulation. We count the number of clones that contain at least one viable cell when radiotherapy ends,

because only these surviving clones are capable of eventually taking over their niches. Their number is determined by the probability $F(k)$ that a live stem cell initiated by the kth dose-fraction produces a clonal lineage, which survives all subsequent dose-fractions. Using analytic results on stochastic birth–death processes with variable rates the Appendix derives an equation, (22), for $F(k)$, which is repeated here:

$$F(k) = \frac{1}{\Delta(k)}, \quad \text{where } \Delta(k) = n^{+}(k)\left[1 + \sum_{j=k}^{K} \frac{n^{-}(j-1) - n^{+}(j)}{n^{-}(j+1)n^{+}(j)}\right].$$

Here, $F(0)$ is the probability that a pre-malignant cell that was present before irradiation began produces a lineage which survives all dose-fractions.

Using the facts that a random thinning of a Poisson distribution is Poisson and the sum of independent Poisson distributions is Poisson, one can show that the total number of surviving pre-malignant clones at the end of the short-term period is Poisson distributed. The above arguments give the mean value as $N_{init} = aXISf(D)$, where D is the total radiation dose (i.e., the sum of all doses per fraction, dK) and $ISf(D)$ (units = dose) represents a net outcome of initiation, inactivation, and cell repopulation during exposure,

$$ISf(D) = \sum_{k=1}^{K} I(k)F(k).$$

The probability that a pre-malignant niche that was present before exposure is not inactivated by radiation (i.e., that at least one pre-malignant stem cell in the niche survives) is given by:

$$Sf(Z, D) = 1 - [1 - F(0)]^{Z} \tag{11}$$

Unifying short- and long-term processes

The above short-term processes are regarded as effectively instantaneous relative to the long-term ones. The stochastic results for the short-term exposure period, in the form of the functions $ISf(D)$ and $Sf(Z, D)$, are inserted into the deterministic equations for long-term carcinogenesis processes. On the long-term time scale, niches already pre-malignant at the end of irradiation and recovery then increase in number by replication; we will refer to all the resulting niches as "old" niches. Other, "new" niches are formed by spontaneous initiation after the end of the exposure period. The contributions of niches in these two categories to the cancer risk are called $N_{rad}E(T_x, T_y)$ and $N_{rad}N(T_x, T_y)$, respectively. At a given time (T_y) after irradiation they are given by the following solutions for (3):

$$\begin{aligned} N_{rad}E(T_x, T_y) &= [(a/b)(\exp[bT_x] - 1)Sf(Z, D) + aXISf(D)]\exp[bT_y] \\ N_{rad}N(T_x, T_y) &= (a/b)(\exp[bT_y] - 1) \end{aligned} \tag{12}$$

Radiation is commonly assumed to promote hyper-proliferation of pre-malignant cells. Here, we interpret this effect as an increase in the number of pre-malignant stem cells per surviving niche above the niche carrying capacity Z, i.e., C becomes >1. For simplicity, the initial excess of C is assumed to be linearly dependent on radiation dose with the coefficient Y (units = dose^{-1}). Promotion may be eventually reversed, because the number of pre-malignant cells per pre-malignant niche may gradually return to pre-irradiation carrying capacity Z. This process may occur concurrently with extinction of some radiation-induced niches. Since only the product of the number of niches and the number of cells per niche is relevant for cancer risk (1), extinction of some niches and/or shrinkage of niche size do not need to be modeled separately. The net effect—i.e., a gradual reversal of promotion—can be modeled using only one adjustable parameter (δ), as done here. According to these assumptions, at any given time (T_y) after exposure to radiation the average normalized number of pre-malignant cells per surviving niche ($C_{rad}(T_x, T_y)$) can be calculated by solving (4):

$$C_{rad}(T_x, T_y) = (1 + YD)/[1 + YD(1 - \exp[-\delta T_y])] \tag{13}$$

Calculation of absolute and relative cancer risks

The approximation for the absolute cancer risk after radiation ($A_{rad}(T_x, T_y)$) can now be calculated at any age at exposure and time since exposure by using the equations above:

$$A_{rad}(T_x, T_y) = [N_{rad}E(T_x, T_y)C_{rad}(T_x, T_y) + N_{rad}N(T_x, T_y)]P(T_x, T_y) =$$
$$\frac{a}{b}\left[\frac{(\exp[bT_x] - 1)Sf(Z, D) + bXISf(D)\exp[bT_y](1 + YD)}{1 + YD(1 - \exp[-\delta T_y])} + \exp[bT_y] - 1\right]\exp\left[-c(T_x + T_y)^2\right] \quad (14)$$

The excess relative cancer risk (ERR) follows from (6) and (14): ERR = $[A_{rad}(T_x, T_y)/A_{bac}(T_x, T_y)] - 1$. By substitution and simplification, a more explicit expression for the ERR can be obtained:

$$\text{ERR} = [(Q_1Q_2 + Q_3)/Q_4] - 1, \quad \text{where}$$
$$Q_1 = (1 + YD)/[1 + YD(1 - \exp[-\delta T_y])];$$
$$Q_2 = [(\exp[bT_x] - 1)Sf(Z, D) + bXISf(D)]\exp[bT_y]; \quad (15)$$
$$Q_3 = \exp[bT_y] - 1;$$
$$Q_4 = \exp[b(T_x + T_y)] - 1$$

Note that the senescence parameter (c) cancels out of this ERR expression; due to the way we have defined our radiation initiation parameter (X), the spontaneous initiation parameter (a) also cancels out. The term Q_1 can be interpreted as the normalized size of old pre-malignant stem cell niches. Q_2 is proportional to the number of such niches. Q_3 is proportional to the number of new pre-malignant niches, and Q_4 is proportional to the total number of pre-malignant niches under background conditions.

Results

To display the properties of the model, we produced Figs. 4–7 using generic parameter values guided by the best-fit values for specific cancer sites found in the accompanying paper.

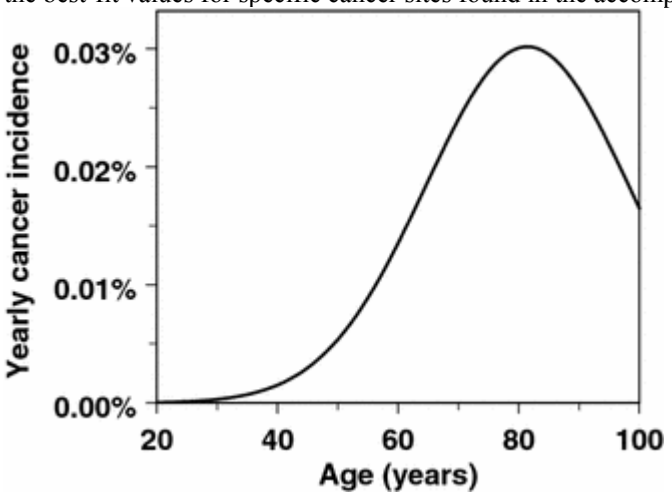

Fig. 4 The typical shape for age dependence of background incidence for a specific type of adult-onset solid cancer is reasonably reproduced by our model. The curve was generated using the following parameter values: $a = 1.0 \times 10^{-8}$ y^{-2}, $b = 0.25$ y^{-1}, $c = 1.75 \times 10^{-3}$ y^{-2}, $L = 10$ y

Figure 4 shows an example of a model-generated age-dependent background incidence curve for an adult-onset solid cancer, using the four relevant parameters a, b, c, and L. The shape of this curve agrees well with the data for many cancers (e.g., SEER database, http://seer.cancer.gov), including the downturn in incidence at old age, which is not described as well by standard models.

Figure 5 shows a typical radiation dose–response, which is determined by the balance of cell initiation, inactivation (killing), and repopulation. Fractionation of the dose increases cancer ERR because

repopulation of both normal and pre-malignant cells during the inter-fraction intervals compensates for much of the cell killing.

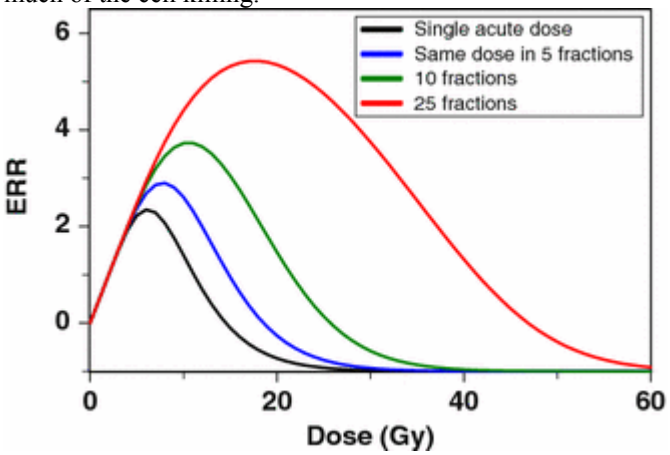

Fig. 5 The effect of dose-fractionation on predicted excess relative cancer risk (ERR): as the same total radiation dose is split into fractions (one fraction per day, with gaps on weekends), thereby protracting it over a longer time, cancer risk predicted by the model increases. This occurs because cell repopulation during prolonged exposure partially compensates for cell killing by radiation. The doses refer to a given organ, such as the lungs or female breast, and not to whole body exposures. The following parameter values were used: $b = 0.25\ \mathrm{y}^{-1}$, $X = 10.0\ \mathrm{y} \times \mathrm{Gy}^{-1}$, $Y = 0.5\ \mathrm{Gy}^{-1}$, $\delta = 0.01\ \mathrm{y}^{-1}$, $Z = 10.0$ cells/niche, $\alpha = 0.3\ \mathrm{Gy}^{-1}$, $\beta = 0.0\ \mathrm{Gy}^{-2}$, $\lambda = 0.35\ \mathrm{day}^{-1}$, $T_x = 30$ y, $T_y = 0.0$ y, and $L = 10$ y

---

Figures 6 and 7 show the effects of age at exposure and time since exposure. The components of cancer ERR produced by radiation-induced initiation and radiation-induced promotion exhibit very different dependences on age at exposure. Radiation is assumed to initiate the same number of cells per unit dose independent of age, whereas the background number of pre-malignant cells, which is essentially the denominator of ERR, grows with age. Consequently, the initiation-driven component of ERR decreases with age at exposure. This process dominates the ERR for ages <20 years in Fig. 6. In contrast, promotion is assumed to be a multiplicative amplification of the background number of pre-malignant cells per niche. Consequently, the promotion-driven component of ERR is approximately constant over most ages at exposure. This process dominates the ERR for older ages in Fig. 6.

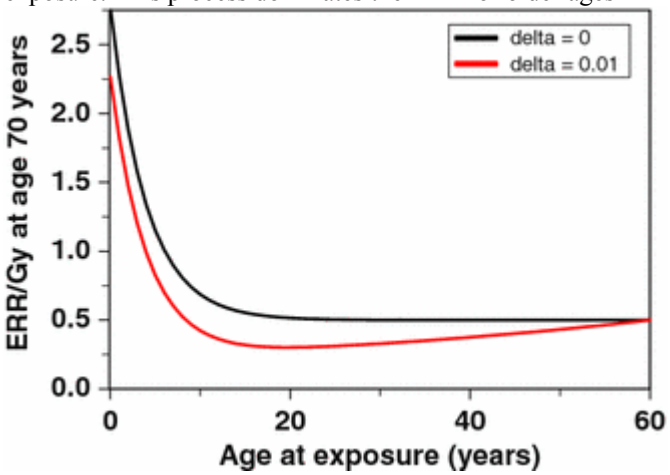

Fig. 6 Combined effects of age at exposure and time after exposure on radiation-induced excess relative cancer risk (ERR). The ERR is calculated at age 70, which is intended to approximate lifetime risk. As discussed in the text, only age at exposure matters if parameter $\delta = 0$, but if $\delta > 0$, time after exposure affects the ERR as well. The parameter values were the same as in Fig. 5, except for T_x and T_y, and a reference radiation dose of 1 Gy

---

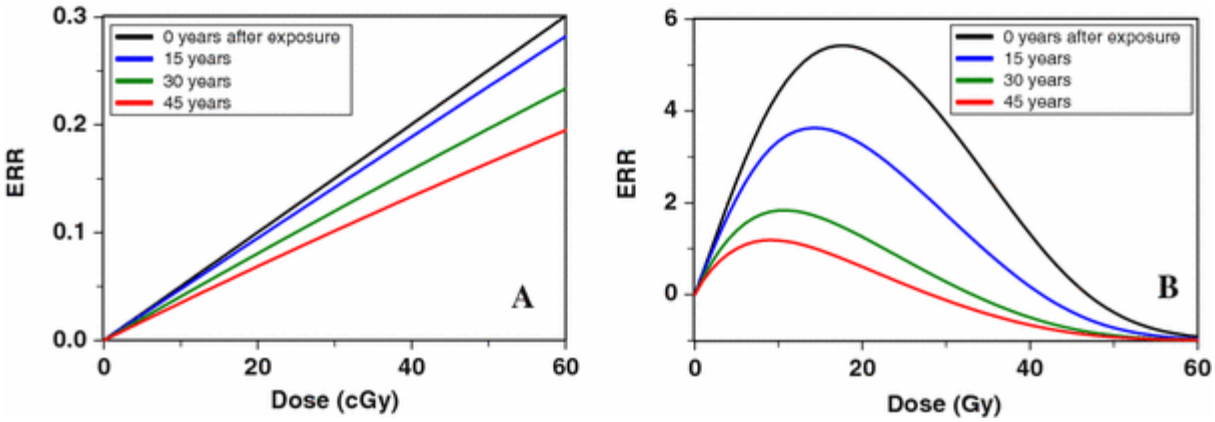

Fig. 7 Modulation of promotion-driven excess relative cancer risk (ERR) over time after exposure: a low doses (either acute or fractionated produce similar results, since cell inactivation is negligible), b high fractionated doses (fractions are given once daily, with gaps on weekends). It is seen that, contrary to a proportional hazards assumption, not only the amplitude but also the shape of the dose–response curve is altered by long-term processes. The parameters were the same as in previous figures

---

Promotion-driven ERR can also be modulated by time after exposure. This occurs due to the assumption that the number of pre-malignant cells per niche is homeostatically regulated (by parameter δ), so that radiation-induced hyper-proliferation of cells within their niches can be reversed, as pre-irradiation cell birth/death rates, and hence niche sizes, are restored. If $\delta > 0$, ERR due to promotion will decrease over time following exposure. This effect is seen in Figs. 6, 7: If the risk is measured at some constant age (e.g., 70 years), which is a sum of age at exposure and time since exposure, a decrease in ERR with time since exposure due to a $\delta > 0$ will appear as an increase in the ERR with age at exposure (Fig. 6). A decrease in promotion-driven ERR with time since exposure also can have a conceptually important effect on the dose–response—at longer times after exposure, not only the magnitude, but also the shape, of the dose–response can change (Fig. 7).

Discussion

The formalism presented here is the first comprehensive attempt to unify short- and long-term modeling approaches. The short-term part of the model belongs to the previously discussed *iir* category. It tracks the numbers of pre-malignant cells throughout irradiation stochastically. The long-term part of the model builds on the concepts developed in previous two-stage formalisms by adding an analysis of some aspects of tissue architecture (i.e., stem cell niches/compartments) and aging of pre-malignant stem cells. The particular short and long-term models that we have chosen to use are not crucial—the real issue is the integration. Certainly other long-term models could perfectly well be integrated into this short-/long-term framework—and we hope they will be.

The unified formalism has a number of advantages. The short-term part can generate reasonable predictions even at high doses, such as those in cancer radiotherapy. The long-term part analyzes the entire lifetime of the individual, putting the short-term predictions in an appropriate context by estimating the effects of age at exposure and time since exposure. The combined approach therefore allows the dose–response for the number of pre-malignant cells to be examined at any time point, from the start of irradiation until development of cancer years to decades later, which is not possible using either short- or long-term models alone.

Our model can be used for estimating risks of second malignancies induced by radiotherapy. This issue is growing in importance as patients are treated earlier in life and the number of cancer survivors increases; the lifetime risk of radiation-induced second cancers is not negligible. Direct measurement of second

cancer incidence requires decades of follow-up because the latency period for radiogenic solid tumors is long. Meanwhile, radiotherapy protocols are rapidly changing. Our model, calibrated using data from older protocols, can produce risk predictions for any modern or prospective radiotherapeutic protocol. This application of the model is discussed in the accompanying paper.

Appendix

This appendix gives some details on the equations for the short-term calculation and on their derivation. We first analyze repopulation effects for normal stem cells deterministically (16–18); then we analyze survival probabilities for pre-malignant clones stochastically. The equations derived are extensions of results given previously.

Normal stem cell numbers

Denote the time of the kth dose-fraction by $T(k)$. We will derive recursive equations valid for $k = 1,\ldots, K$, where the number of fractions is K as in the main text. We formally define $T(K + 1) \equiv \infty$; this infinite value represents the end of the recovery period (Fig. 1). It reflects a standard procedure in multi-timescale analyses, an infinite time interval in a short-timescale model represents a short time interval in the next larger timescale model (here several months in our long-timescale model). We correspondingly set $n^{-}(K + 1) = \nu$, the set point value attained at the end of the recovery period.

Solving (9) of the main text gives $n(t)$ for any time t after the kth dose-fraction and before the $(k + 1)$st:

$$n(t) = \frac{n^{+}(k)\nu}{n^{+}(k) + [\nu - n^{-}(k)]\exp[-\lambda[t - T(k)]]}, \quad \text{for} \quad T(k) < t < T(k+1) \tag{16}$$

In particular, for $n^{-}(k + 1)$, 16 gives:

$$n^{-}(k+1) = \frac{n^{+}(k)\nu}{n^{+}(k) + [\nu - n^{-}(k)]\exp[-\lambda[T(k+1) - T(k)]]}. \tag{17}$$

Normal stem cell number $n(t)$ can be calculated recursively for all times by combining the proliferation equations, (16) and (17), with the survival equation discussed in the main text:

$$n^{+}(k) = S(k)n^{-}(k), \quad \text{where } S(k) = \exp[-\alpha d - \beta d^2]. \tag{18}$$

Pre-malignant stem cell clones

To analyze pre-malignant clones stochastically, consider a clone that starts with a single live stem cell initiated by the kth dose-fraction, and is followed in time. The time evolution of the clone is modeled as a time inhomogeneous birth–death process with birth rate $b(t)$ and death rate $r(t)$. The appropriate death rate, taking the spontaneous death rate as zero to minimize the number of adjustable parameters, is the death rate due to the dose-fractions, namely

$$r(t) = \sum_{k=1}^{K} [\alpha d + \beta d^2]\,\delta[t - T(k)], \tag{19}$$

where $\delta[t]$ is the Dirac delta function.

Equation (19) corresponds to the statements that on average the surviving cell fraction for the kth dose-fraction is given by (18) and that pre-malignant stem cells have the same radiosensitivity to inactivation as do normal stem cells. By our assumption that, during the comparatively short radiotherapy and recovery periods, normal and pre-malignant cells have effectively the same proliferation rate, the appropriate birth rate is

$$b(t) = \lambda(1 - [n(t)/\nu]) \tag{20}$$

In (20) $n(t)$ is a known function of time, determined as discussed above.

It is well known that by integrating an appropriate partial differential equation for the probability generating function one can deduce the following expression for the probability $F(k)$ that the pre-malignant clone survives all subsequent dose-fractions:

$$F(k) = 1/(\xi + \zeta), \text{ where}$$

$$\psi(t) = \exp\left[\int_{T^+(k)}^{t} [r(u) - b(u)]\,du\right], \quad \xi = \psi(T^+(K)), \quad \text{and } \zeta = \int_{T(k)}^{T(K)} b(t)\psi(t)dt. \tag{21}$$

Here, $T^+(k)$ denotes the time just after the kth fraction. Because of the way a Dirac δ function behaves, using T^+ rather than T is important in the expressions for ψ and ξ.

Performing the integrals in (21) with the help of (16–20) gives, after a quite long, but routine, calculation, the following convenient equation for the clone survival probability $F(k)$:

$$F(k) = \frac{1}{\Delta(k)}, \quad \text{where } \Delta(k) = n^+(k)\left[1 + \sum_{j=k}^{K} \frac{n^-(j-1) - n^+(j)}{n^-(j+1)n^+(j)}\right]. \tag{22}$$

Equation (22) is valid for $k = 0, 1, \ldots, K$, with $k = 0$ referring to pre-malignant cells present before radiation starts and $F(K) = 1$. It is the primary mathematical result needed for the data analysis discussed in the main text.

We have some extensions, not needed in the present paper. Generalizing to situations where the spontaneous death rate is non-zero and/or one needs the probability that a clone has a given number of cells at the final time, can readily be done by using results given by Tan. In addition, it can be shown that (22) holds even if the recovery equation for normal cells is different from the logistic equation used in this paper, e.g., is Gompertzian.

III. The Relationship Between the Inverse Dose Rate Effect and the Bystander Effect

Summary

The effectiveness of high-LET radiation per unit dose increases as dose rate decreases. This "inverse dose rate effect" is seen in radon-induced lung carcinogenesis. We suggest a biologically-motivated mechanism based on radiation-induced direct and bystander-effect-related risks: During radon exposure, only a fraction of cells are traversed by alpha particles. These irradiated cells have an increased probability of being initiated into a pre-malignant state. They release signals, which convert some nearby unirradiated cells to an activated state. When already pre-malignant cells are activated, their proliferation (promotion) rate increases. If a radiation dose is sufficient to activate most susceptible cells, protracting the exposure does not substantially decrease the number of activated cells, but prolongs the activated state during which pre-malignant cell proliferation is accelerated. This mechanism is implemented in a low-dose-rate extension of our carcinogenesis model, which integrates both short- and long-term modeling approaches, and was applied to radiotherapy-induced second cancer risk estimation. Model predictions adequately describe the data on radon-induced lung carcinogenesis in humans and rats, using few adjustable parameters. Conclusions about the relative importance of promotion vs. initiation for radon carcinogenesis are similar to those reported with the two-stage clonal expansion model, but a mechanistic explanation for promotion is provided.

Biological Motivation for Inverse Dose-Rate Effects Due to the Newly Suggested Bystander Mechanisms

As well as producing explicit DNA damage, radiation (and other stressors) can move (activate) cells into a state of oxidative stress. Cells in this state are more likely to accumulate radiobiological endpoints such as cell killing, mutation, or conversion to a pre-malignant phenotype.

The phenomenon of persistent oxidative stress is thought to arise by several mechanisms. For example, the initial burst of oxidant molecules produced directly by radiation can serve as a trigger for a prolonged process of oxidant overproduction. Oxidant-responsive signaling pathways can spread among groups of neighboring cells through the medium and/or through gap junctions, and this has been suggested as the basis of the so-called bystander effect. These signals may induce oxidative stress (and the consequent elevation in DNA damage) in cells, which have not themselves been irradiated, but are located in proximity to irradiated cells, or have merely been exposed to medium from irradiated cell cultures.

We have suggested that bystander mechanisms may also be (at least partially) responsible for inverse dose-rate effects. In brief, if the same dose of radiation is protracted by using a lower dose rate, because of saturation effects, the number of activated cells may not decrease, but the duration of the activated state is prolonged, thereby increasing the yield of endpoints such as pre-malignant cells. Implementation of this hypothesis in the form of a new mathematical model is based on the following main assumptions:

1. Cells do not need to be directly traversed by ionizing tracks in order to show increased levels of biological damage – those that are not traversed may become "activated" by damage-response bystander signals released from other nearby (bystander) cells. Most likely the activated state represents a state of oxidative stress, although its actual nature does not need to be specified in order to apply the model.

2. Bystander signals act in a probabilistic binary manner, causing susceptible cells to switch from an undisturbed background state to an activated state. Eventually, after sufficient time following irradiation, activated cells will revert to the background state.
3. Cells in an activated state, *e.g.,* of oxidative stress, are more likely to accumulate radiobiological endpoints such as cell killing, mutation, or conversion to a pre-malignant phenotype, the probability of which will be proportional to the number of activated cells and the time they spend in the activated state.
4. The bystander response is saturable, *i.e.,* an activated cell cannot be further activated. This results in a characteristic downwardly-curving dose-response relation for an acute exposure (*i.e.,* a curve with a negative second derivative). If the radiation is protracted, for a given dose (assuming this dose is not too low), the number of activated cells stays approximately the same due to saturation, but these cells remain in the activated state for a longer time. This will result in an increased yield of, for example, pre-malignant cells – an inverse dose-rate effect.
5. The bystander-induced damage adds to the damage produced by direct traversal of targets by radiation.

New Mathematical Model for the Bystander-Related Inverse Dose-Rate Effect

We have previously argued that a bystander signal at concentration S acts in a probabilistic binary manner, causing susceptible cells to switch from an undisturbed background state to an activated state (*e.g.,* increased oxidant production), resulting in elevated rate of DNA damage accumulation. This assumption was based on experimental results suggesting that excess damage in bystander cells is approximately dose-independent over a broad range of radiation doses, *i.e.* "on or off" in quality.

More specifically, we assumed that a susceptible cell will have a probability P_a of being in the activated bystander state, rather than in the background bystander state, with P_a described by the following differential equation:

$$dP_a/dt = c_2 S (1 - P_a) - c_3 P_a \qquad \text{Eq. 1}$$

Here c_2 and c_3 are rate constants for transition between the two states: c_2 determines the rate at which the activated state is induced, and c_3 determines the rate of the opposite process, where activated cells revert back to background. The term $c_2 S$ represents our assumption that the probability per unit time of converting a cell from the background state to the activated state is proportional to the concentration of the bystander signal (S). The term $1 - P_a$ indicates the probability that the given cell has not yet undergone this transition and is therefore available for being activated by the bystander signal, and thus describes the "saturation" phenomenon characteristic of bystander. Finally, the term $-c_3 P_a$ represents the assumption that the activated state tends to spontaneously revert to background at a fixed probability per unit time.

In the present paper we will again use Eq. 1. We will assume here that the time-average over a short time (*e.g.,* a day) of the signal concentration, S, rapidly (essentially instantaneously on the relevant time scale of months and years, on which typical exposure to radon occurs) reaches a steady-state value, which is linearly proportional to the radiation dose rate, R. This assumption can be derived from the plausible supposition that each cell traversed by an ionizing track sends out the bystander signal briefly. During protracted irradiation, cells are hit at random continually. Thus, at any location the time average of S over a characteristic relaxation time T_c (*i.e.,* the time needed to revert from activated state to background state, $T_c = 1/c_3$) is spatially and time independent (after the initial and before the final transients, which are assumed to be short), and is proportional to R.

This assumption would be less likely to hold at high dose rates, where most or all cells are traversed at least once per relaxation time (T_c). However, at such high dose rates, essentially all cells susceptible to activation by bystander signals would be activated ($P_a = 1$), so any deviation of the dependence of signal concentration on dose rate from linearity (*e.g.,* saturation of signal production) would not affect model predictions.

This scenario can be represented mathematically as

$$S = \rho R, \qquad \text{Eq. 2}$$

where ρ is a proportionality constant. Defining a new parameter $k_1 = c_2 \rho$, Eq. 1 can thus be rewritten as:

$$dP_a/dt = c_2 \rho R (1 - P_a) - c_3 P_a = k_1 R (1 - P_a) - c_3 P_a. \qquad \text{Eq. 3}$$

The constant k_1 is an indirect measure of the spatial range and efficiency of bystander signaling. For example, consider the case when the bystander signal range is large, so that one directly hit cell can activate susceptible cells within a large radius (*e.g.,* >100 μm). Comparatively few hit cells located far apart can activate all the remaining susceptible cells within the tissue. In the context of Eq. 3, such a situation is produced by a large value of k_1, *i.e.,* the product $k_1 R$ becomes large compared to c_3 even at low values of the dose rate, R. By contrast, consider the case when the signal range is small, so that only the immediate neighbors of directly hit cells can be activated; this implies a small value of k_1, meaning that a relatively high dose rate (*e.g.,* almost one traversal per cell during one characteristic time T_c, on average) would be required to activate all susceptible cells.

An analytic solution for Eq. 3 is available. However, to simplify the final model, it is possible to approximate by using the equilibrium condition $dP_a/dt = 0$, and solving for P_a. The equilibrium value of P_a is:

$$P_e = 1/[1 + c_3/(k_1 R)]. \qquad \text{Eq. 4}$$

This approximation is useful in situations, typical of those of interest here, where the irradiation time is long (several years) compared with: (1) the characteristic time needed for a cell to be activated (T_a) after it is exposed to bystander signals, which is typically on the order of minutes to hours; and (2) the characteristic time needed for activated cells to return to background state (*i.e.,* $T_c = 1/c_3$), which is

typically on the order of many hours to weeks, depending on cell type. A schematic representation of these processes is shown in Fig. 1.

Fig. 1. Diagrammatic representation of cell activation probability (P_a). The time (T_a) needed for P_a to reach an equilibrium concentration (P_e), and the time (T_c) needed for P_a to return to zero after radiation is over, are both typically much shorter, than the time during which radiation is acting (T_{rad}).

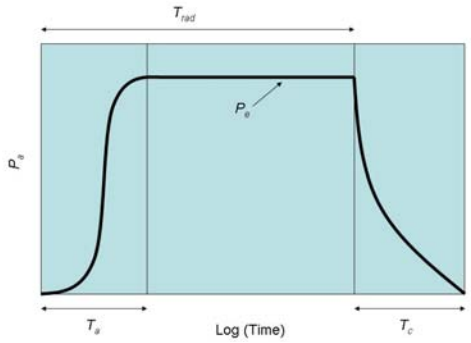

It is important to point out that the situation of radon exposure, which is modeled here, is substantially different from the situation of high-dose acute α-particle exposure in vitro, which we analyzed in our spatial bystander model. In the in vitro scenario, 10 α-particles per cell were delivered by a microbeam only to a thin slice of tissue over a period of about 1 minute, and damage (apoptosis and micronucleation frequencies) was scored in the bystander cells located at various distances perpendicular to the exposed slice 72 hours after irradiation. This experiment was specifically designed to investigate spatial propagation of the bystander effect, and not its temporal kinetics. Its short duration implies that the main process being observed was initial cell activation. In other words, the experiment was essentially confined only to the initial time interval T_a in Fig. 1. Cell deactivation (with rate c_3), which operates on a longer time scale, was largely irrelevant in this instance, and was neglected in our analysis, which concentrated on signal propagation kinetics by the "fire-diffuse-fire mechanism".

In contrast, the typical situation of radon exposure (which is modeled here) is that of continuous low dose rate irradiation over multiple years (in humans). The total dose is much lower, than that in the in vitro situation, so that hardly any cell is hit by more than one α-particle throughout its lifetime. The α-particle tracks are deposited effectively randomly throughout the tissue, so that they can be considered spatially homogenous on a large scale. In this case, the bystander signal concentration is assumed to be spatially homogeneous as well, and details of spatial propagation can be neglected. Temporally, the signal is assumed to be in steady-state, because the duration of radiation exposure (years) is much longer than both the rates of cell activation and cell deactivation. In other words, most of the radiation-induced risk is expected to be determined by processes occurring during the long time period throughout radiation exposure, when the bystander signal concentration is essentially at equilibrium (the time interval $T_{rad} - T_a$ in Fig. 1). For the equilibrium concentration (P_e) to be estimated, the rate of deactivation (c_3) cannot be neglected, as in our spatial bystander model, and is taken into consideration here.

To reduce the number of parameters, Eq. 4 can be written as:

$$P_e = 1/(1 + k/R). \qquad \text{Eq. 5}$$

Here the parameter k ($= c_3/k_1$) is the ratio of cell deactivation to cell activation constants, with units of dose rate (*i.e.,* dose/time). It is an adjustable parameter, the value of which is determined by multiple factors such as bystander signal range (which affects k_1) and cell turnover rate (which affects c_3). If k is small, P_e approaches saturation (unity) at lower dose rates than when k is large. By definition, when $R = k$, $P_e = ½$.

According to our Assumption 3, the yield of excess activation-induced damage is proportional to the number of activated cells and the time they spend in the activated state, *i.e.,* the time integral (I) of the cell activation probability. Using the equilibrium approximation for activation probability from Eq. 5, the time integral over the irradiation time, $t=D/R$, where D is total dose, is:

$$I = t\,P_e = t/(1+k/R),$$

$$= D/(k + R). \qquad \text{Eq. 6}$$

The structure of Eq. 6 is consistent with the previously given intuitive explanation for the inverse dose-rate effect. The slope of the dose response (I/D) is equal to $1/(k + R)$. Clearly, the value of this slope varies inversely with dose rate – as R decreases, $1/(k + R)$ increases.

It is pertinent to point out that any sub-linear acute dose response relation (*i.e.,* a curve with a negative second derivative), independent of the underlying model, will presumably generate some degree of inverse dose rate effect. This can be demonstrated by mimicking a decrease in dose rate by splitting the dose into two equal fractions: If the dose response is linear (*i.e.,* its second derivative is zero), the sum of the responses to both fractions would be the same as the response to the total dose (no dose rate effect). If the dose response is upwardly curving (*i.e.,* its second derivative is positive), the sum of the responses to both fractions would be smaller than the response to the total dose (a direct dose rate effect). However, if the dose response is downwardly-curving (*i.e.,* it second derivative is negative), the sum of the responses to both fractions would be greater than the response to the total dose (an inverse dose rate effect).

Derivation of Equations for Bystander + Directly-Induced Cellular Initiation

According to our assumption 5, activation-induced damage adds to the damage produced directly by radiation. Both types of damage contribute to initiation of target cells (*i.e.,* conversion of normal cells to pre-malignant ones). This implies the following form for the initiation rate function, $F_i(R,t)$:

$$F_i(R,t) = a\,R + c\,P_a \qquad \text{Eq. 7}$$

Here a is a linear initiation term for direct radiation action, and c is the maximum initiation term due to bystander effects. Using Eq. 5 as an approximation for P_a, the explicit expression for the initiation rate is thus:

$$F_i(R,t) = a\,R + c/(1 + k/R) \qquad \text{Eq. 8}$$

The excess relative risk (ERR) can be calculated by integrating Eq. 8 over time, until the time when radiation exposure ends ($t = D/R$). The solution is:

$$ERR = (a + c/[k + R])\,D \qquad \text{Eq. 9}$$

This model has three adjustable parameters: a (units: dose^{-1}), c (units: time^{-1}), and k (units: dose/time). If $a = 0$, the implication is that there is no direct initiation by radiation, and all initiation is due to cell bystander signaling. This scenario may be realistic only at extremely low dose rates. If $c = 0$, the implication is the opposite – that there is no initiation due to cell activation. This scenario may be realistic at high dose rates, where damage induction by cell activation would be negligible because of the large amount of directly-induced damage, depending on cell and radiation type. If $k = 0$, the implication is that initiation due to bystander signaling saturates to its maximum value (c) at extremely low dose rates. This scenario can be approached, for example, in situations where k_1 is large (*e.g.,* the spatial range of bystander signals is large), and/or c_3 is very small (*e.g.,* it takes a long time for cells to revert from the activated state to the background state).

Limiting Cases and Approximations of the Initiation-Only Model

The overall behavior of the initiation-only model can be seen by approximating Eq. 9 under limiting conditions of very low or very high dose rates:

a) When $R = 0$, *i.e.,* at very low dose rates, Eq. 9 simplifies to:

$$ERR = (a + c/k)\,D. \qquad \text{Eq. 10}$$

Thus, the slope of ERR per unit dose (ERR/D) at very low dose rates is predicted to be equal to $a + c/k$ at all doses.

b) When R = infinity, *i.e.,* at very high dose rates, Eq. 9 simplifies to:

$$ERR = a\,D. \qquad \text{Eq. 11}$$

Thus, the predicted slope of ERR per unit dose at high dose rates is equal to a at all doses.

Estimating the Contributions to Total ERR from Bystander and Direct Effects

The ERR due to bystander effects (ERR_b) can be calculated by setting the direct initiation rate constant a to zero in Eq. 9:

$$ERR_b = c\,D/[k + R]. \qquad \text{Eq. 12}$$

Thus, the fraction of the total ERR caused by bystander effects (ERR_b/ERR) can be determined by dividing Eq. 12 by Eq. 9, as

$$ERR_b/ERR = 1/(1 + a/c\ [k + R]). \qquad \text{Eq. 13}$$

Eqs. 12 and 13 indicate that the bystander effect plays the most important role at low dose rates, and at high dose rates direct effects begin to dominate. The absolute contribution of the bystander effect (ERR_b) depends on both dose and dose rate, whereas the fractional contribution (ERR_b/ERR) depends on dose rate only. The characteristic dose rate at which the bystander effect and the direct effect account for equal risks is given by:

$$R_{0.5} = c/a - k. \qquad \text{Eq. 14}$$

Fitting the Initiation-Only Model to Human Lung Carcinogenesis Data

The model described by Eq. 9, which incorporates both bystander-induced and direct cellular initiation, was fitted to lung carcinogenesis data from radon-exposed miners, and data on risks of household exposure to radon. Fitting was performed using a customized random-restart simulated annealing algorithm written in the Fortran language. To avoid skewing the results towards larger doses, where the largest ERR values were generally observed, ERR/100 WLM, rather than total ERR, was used in the fitting procedure. Each point was assigned a weight inversely proportional to the width of its 95% confidence intervals. The results were plotted both as ERR per unit dose as function of dose rate (showing the inverse dose rate effect, Figs. 2-3), and as total ERR as function of dose for several dose rate categories (showing the linear dose response at each constant dose rate, Fig. 4).

The best-fit parameter combination was: $a = 2.253 \times 10^{-3}$ WLM^{-1}; $c = 1.635 \times 10^{-2}$ WLM/WL, $k = 1.007$ WL. The quality of the fit was adequate for all data.

Biological Motivation for Modeling Promotion of Pre-Malignant Cells

As discussed previously, the initiation-only model provides a reasonable description of the human data, both as a function of dose rate, and as a function of dose – in particular, showing a linear increase in risk for a fixed dose rate. However, at the extremely high doses that were used in the investigations of radon-induced lung cancer in rats (PNNL, AEAT and CEA studies), for a given dose rate, the lung cancer risks appear to increase with dose in a super-linear way (*i.e.,* the risk per unit dose at a constant dose rate has a positive second derivative), although the F-test for non-linearity was not significant. As discussed by Heidereich *et al.*, this super-linear increase in risk may be evidence for the effects of promotion. We model here a mechanistic interpretation of such a promotion effect, in term of cell killing which causes an acceleration of tissue turnover. Specifically, pre-malignant cells are assumed to have a slight competitive advantage in term of re-growth, and thereby expand in number.

This picture of cell killing and compensatory proliferation can be represented by the following differential equation:

$$dn/dt = -\alpha R n + \delta n (1 - n). \quad \text{Eq. 15}$$

Here n is the total number (or density) of cells in the tissue, normalized relative to the homeostatically controlled number under background conditions (*i.e.,* without any radiation exposure $n = 1$), α is a radiation-induced cell killing constant, and δ is the maximum cell proliferation rate. The term $\delta n (1 - n)$ is an expression for logistic growth – it implies that without any radiation, when $n = 1$, there is no cell proliferation, but as soon as n drops below unity due to cell killing by radiation, compensatory proliferation begins. The background proliferation rate without radiation is neglected for purposes of simplifying the model, to avoid extra adjustable parameters. This assumption should hold reasonably well for tissues where the background stem cell turnover rate is relatively slow, such as in the lung, and may be less applicable to tissues with rapid turnover rates, such as the colon. Eq. 15 is intended to apply to normal (not pre-malignant) cells, which are expected to make up the vast majority of cells in the tissue. The kinetics of pre-malignant cells will be discussed below as a modification of normal cell kinetics.

Under the conditions of prolonged low dose rate irradiation which are of interest here, n will approach the equilibrium condition where $dn/dt = 0$, because killing and proliferation will cancel each other out (assuming the dose rate is not high enough to overpower proliferation). The equilibrium cell number (n_e) can be found by setting $dn/dt = 0$, and solving for n in Eq. 15. The solution is:

$$n_e = 1 - \alpha R/\delta. \quad \text{Eq. 16}$$

The cell proliferation rate when $n = n_e$ can be derived by substituting n_e in place of n in the logistic term of Eq. 15. This rate, r, is

$$r = \delta n_e (1 - n_e) = \alpha R - (\alpha R)^2/\delta. \quad \text{Eq. 17}$$

For low dose rates, $R^2 \ll R$, so $\alpha R \gg (\alpha R)^2/\delta$. As an example, consider the plausible situation where $\alpha = 1.0$ Gy^{-1}, $\delta = 1.0$ $month^{-1}$, and $R = 0.1$ Gy/month. Using these values, $\alpha R = 0.1$ $month^{-1}$, and $(\alpha R)^2/\delta = 0.01$ $month^{-1}$, so $\alpha R = 10\ (\alpha R)^2/\delta)$. This implies that Eq. 17 can be simplified by neglecting the term $(\alpha R)^2/\delta$, and that the normal cell proliferation rate can be approximated by $r = \alpha R$.

Pre-malignant cells are assumed to have some growth advantage over normal cells, so their proliferation rate (r_p) is given by the expression $r_p = m\, r = m\, \alpha\, R$, where $m > 1$. This expression can be simplified by defining $\lambda = m\, \alpha$, thereby removing one adjustable parameter. The result is:

$$r_p = \lambda R, \quad \text{Eq. 18}$$

where λ is a net promotion rate for pre-malignant cells per unit dose. Eq. 18 implies that a cell that is initiated (*i.e.,* becomes pre-malignant) at time t is expected to produce $\exp[\lambda R (T - t)]$ viable descendants at time T, where $T > t$. (We explicitly consider only cells that are initiated by radiation, either directly, or by

indirect (*e.g.,* bystander) mechanisms, and neglect any background pre-malignant cells present before irradiation). Thus, the radiation-induced promotion function for pre-malignant cells ($F_p(R,t)$) is given by:

$$F_p(R,t) = \exp[\lambda\, R\, (T - t)] \qquad \text{Eq. 19}$$

The final time T can be conveniently defined as the time when radiation stops (*i.e.,* $T = D/R$), since after that time $R = 0$, so that no more promotion is expected to occur ($F_p(R,t) = 1$).

When $T \gg t$, the promotion term is $\exp[\lambda\, R\, T] = \exp[\lambda\, D]$. It may be noted that: a) this promotion term is non-linear (super-linear) in dose, and b) in this approach the promotion effect is independent of dose rate; this biologically motivated model of promotion is thus in contrast to the approach described by Heidenreich *et al.*, in which the promotion term is dose-rate dependent, achieved essentially through introducing an "ad-hoc" dose rate dependence for the proliferation parameter, λ.

Combining Initiation and Promotion into One Initiation+Promotion Model

The excess relative cancer risk (ERR) is assumed to be proportional to the excess number of mutant cells at the time when radiation ends (T). It is given by the following general equation, where $F_i(R,t)$ is cell initiation as function of radiation dose rate (R) and time (t), and $F_p(R,t)$ is radiation-induced promotion of initiated cells:

$$ERR = \int_0^T F_i(R, t)\, F_p(R, t)\, dt \qquad \text{Eq. 20}$$

Substituting Eq. 9 for initiation, and Eq. 19 for promotion into Eq. 20 and integrating, it is possible to get an analytic solution for ERR. Assuming that the time when radiation stops is defined as $T = D/R$, where D is the total radiation dose, the solution is:

$$ERR = (a/\lambda + c/[\lambda\, (R + k)])\, (\exp[\lambda\, D] - 1) \qquad \text{Eq. 21}$$

Fitting the Initiation+Promotion Model to Rat Lung Carcinogenesis Data

The model described by Eq. 21, which incorporates dose-dependent promotion in addition to bystander-induced and direct initiation, was fitted to lung carcinogenesis data from radon-exposed rats (PNNL, AEAT and CEA studies). The data were split into two data sets: (1) the PNNL data, and (2) pooled CEA and AEAT data. Such a split was done by us, as well as by Kaiser *et al.*, because background lung cancer incidence is very different (by several-fold) between the Wistar-strain rats used by the PNNL study, and the Sprague-Dawley-strain rats used by the CEA and AEAT studies, so that ERRs per unit dose are also very different for these two strains.

Fitting was performed using the same algorithm and procedure, as for the human data discussed earlier. Parameters a, k, and λ were kept constant for both data sets, and only parameter c was allowed to have different values for the different data sets. Each data set was weighted by the inverse sum of all data points (*i.e.,* the sum of all ERR / 100 WLM values), so that both data sets (and not individual points) had

equal weight. This was done to preclude the AEAT and CEA data sets, which together contain more points with larger ERR values than the PNNL data set, from dominating the combined fit. Following the procedure used by Kaiser *at al.*, the data were analyzed without error bars. For presentation purposes, error bars for the PNNL rat data were extrapolated by transferring the relative errors from Heidenreich *et al.* to the data in Kaiser *et al.*.

The best-fit parameters were: $a = 0.0$ ($<1.0 \times 10^{-5}$) WLM^{-1}, $c = 13.80$ WL/WLM (PNNL) and 578.2 WL/WLM (CEA+AEAT), $k = 1174$ WL, $\lambda = 1.465 \times 10^{-4}$ WLM^{-1}. The results are shown in Figs. 5-6.

Results

A comparison of best-fit predictions generated by the initiation-only (linear with dose) model (Eq. 9) to data on lung cancer ERR for humans exposed to radon occupationally (uranium miners) or domestically is shown in Fig. 2. The data are displayed in the form of ERR/100 WLM as function of dose rate (WL), rather than in the form of total ERR as function of dose (WLM), in order to demonstrate the inverse dose rate effect. Although many data points, especially at low dose rates (*e.g.,* < 0.5 WL), have large error bars due to epidemiologic difficulties of risk estimation, the general pattern can be seen that ERR/100 WLM decreases with increasing dose rate by a factor of several-fold over the range of dose rates shown (~ 0.001 – 30 WL). The model fits this pattern adequately, using the following best-fit parameter values: $a = 2.253 \times 10^{-3}$ WLM^{-1}; $c = 1.635 \times 10^{-2}$ WLM/WL, $k = 1.007$ WL. As derived above, at very low dose rates ERR per unit dose is equal to $a + c/k$, from Eq. 10, and at very high dose rates it is equal to a, from Eq. 11. Substituting the best-fit parameter values, this means that ERR/100 WLM = 1.849 at very low dose rates, and 0.2253 at very high dose rates, so that the inverse dose rate effect produces roughly an 8-fold variation in risk per unit dose.

The fractional contribution of the bystander effect to radon-induced ERR, as predicted by the model, is shown in Fig. 3. At low dose rates (*e.g.,* < 1 WL), most of the risk (~ 80-85 %) is caused by the bystander effect. This scenario applies to typical exposure conditions in homes, where radon levels vary from 0.005 to 0.02 WL. Only at much higher dose rates (*e.g.,* > 1 WL) does direct damage induction by α-particle traversals begin to dominate. As derived above (Eq. 14), the dose rate at which bystander and direct effects contribute to ERR equally is $c/a - k$. Using the best-fit parameters, this corresponds to 6.250 WL. Such high dose rates were encountered by uranium miners several decades ago, but are unlikely to be encountered again, considering improvements in safety methods.

The dependence of total ERR on radiation dose (WLM) at a constant dose rate (WL) was estimated by stratifying the data into categories of relatively similar dose rates (*e.g.,* 0.1-0.2 WL, 0.2-0.5 WL, etc.). During the fitting procedure, model predictions were calculated for the exact dose and dose rate combinations for all data points. For presentation purposes (to produce a smooth curve), predictions using best-fit parameters were calculated for mid-interval dose rates within each category (*e.g.,* for 0.2-0.5 WL the mid-interval was 0.35 WL). These predictions, along with the data, are plotted in Fig. 4. Clearly, the linear dose-dependence of total ERR at constant dose rate, which is suggested by Eq. 9, appears to be a good description of the data.

The model was also applied to data from the PNNL and pooled AEAT+CEA rat studies. These experiments with laboratory animals investigated the region of very high dose rates (50 - 1880 WL) and very high doses (2500 – 10000 WLM), which have never been encountered by humans. The best-fit parameters for the rat data were: $a = 0.0$ ($<1.0 \times 10^{-5}$) WLM^{-1}, $c = 20.87$ WL/WLM (PNNL) and 804.4 WL/WLM (CEA+AEAT), $k = 1594$ WL. Parameters a and k were deliberately kept constant for the two data sets to reduce the number of adjustable variables. When this restriction was relaxed, so that different values of a and k were allowed for each data set, their values did not change very substantially (by a factor of <1.5-fold), and the fit was not substantially improved (data not shown).

The best-fit numbers suggest that the contribution of direct initiation to total ERR was small, and could not be resolved from the rat data (hence $a \approx 0$). Of course, this absence of direct initiation cannot be taken at face value, and most likely represents the limited power of the model to fit the data set. The large value of k (1594 WL) contrasts dramatically with the value obtained from the human data (1.007 WL). This may represent true biological differences between rat and human responses to radon, but, more likely, it simply implies that the model was unable to resolve any inverse dose rate effect for the data below about 1000 WL, because the data in this region were highly scattered. The order of magnitude differences in the values of c for the two rat data sets reflect the fact that Sprague-Dawley strain rats used in the AEAT+CEA studies have a much lower spontaneous incidence of lung cancer, than Wistar strain rats used in the PNNL study, so that the ERR per unit dose is correspondingly much higher in the Sprague-Dawley rats.

The rat data suggest that in the region of very high doses (*e.g,* >2500 WLM), ERR may grow faster-than-linearly with dose (*i.e.,* ERR/100 WLM would not be constant at a given dose rate, but would increase with dose). The explanation for this putative non-linearity is promotion of pre-malignant cells. Consequently, the model version incorporating promotion (in addition to direct and bystander-induced initiation, from Eq. 21) was also fitted to the rat data. Parameters a, k and λ were kept constant for the PNNL and CEA+AEAT data sets, because allowing their values to be different for each data set did not improve the fit substantially (data not shown). The best-fit parameter values were: $a = 0.0$ ($<1.0 \times 10^{-5}$) WLM^{-1}, $c = 13.80$ WL/WLM (PNNL) and 578.2 WL/WLM (CEA+AEAT), $k = 1174$ WL, $\lambda = 1.465 \times 10^{-4}$ WLM^{-1}.

Results of the fits of the initiation-only model (Eq. 9) and the version with promotion (Eq. 21) are shown in Figs. 5 and 6. Both versions fit the data reasonably well, and the change in deviance due to the introduction of one extra adjustable parameter (the dose-dependent promotion constant λ) is not very large (deviance decreases by 6.88%). Such a small decrease in deviance is insufficient to make the F-test for non-linearity reach 5% significance.

Fig.2. Measured and predicted ERR/100 WLM. The data points at dose rates >0.04 WL are derived from uranium miners, and those ≤0.04 WL are derived from domestic exposure. Panel A shows the data and model predictions, and panel B shows the model predictions only, rescaled for better visualization of the inverse dose rate effect.

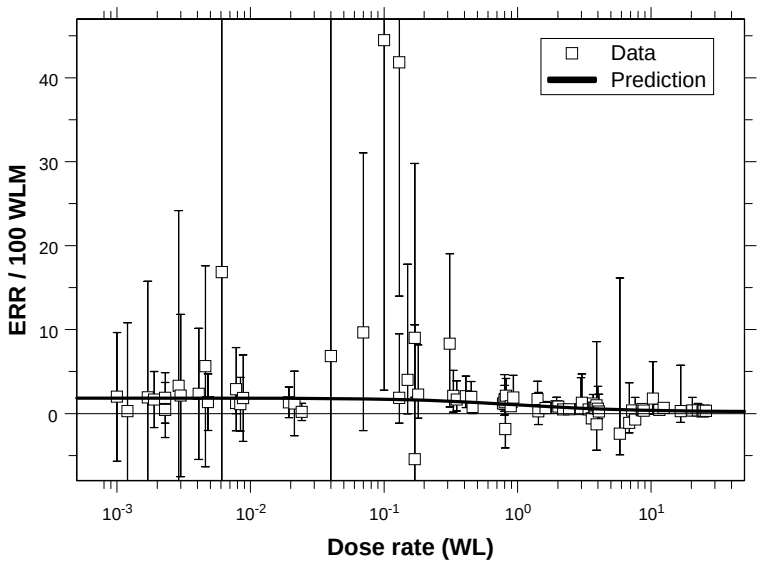

A

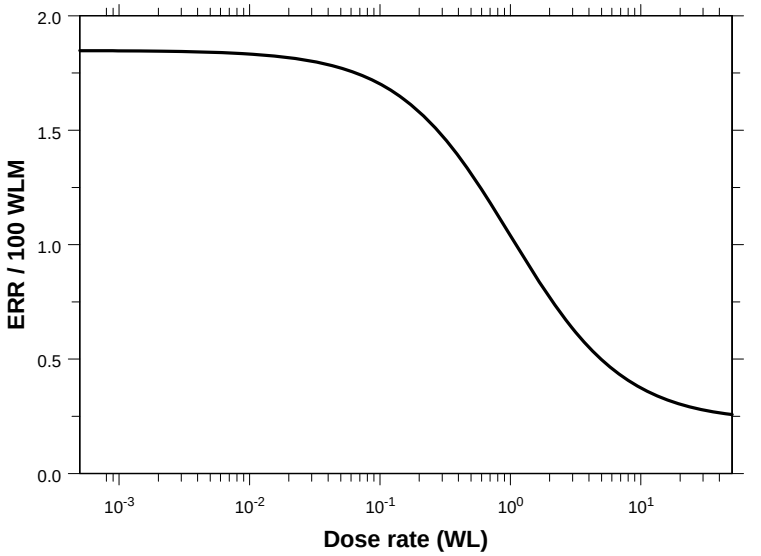

B

Fig. 3. Contributions of bystander and direct effects to total ERR at different dose rates. The average indoor radon level is estimated at 0.005 WL, a high indoor level could be 0.02 WL, and the average exposure level for Colorado uranium miners was 11 WL.

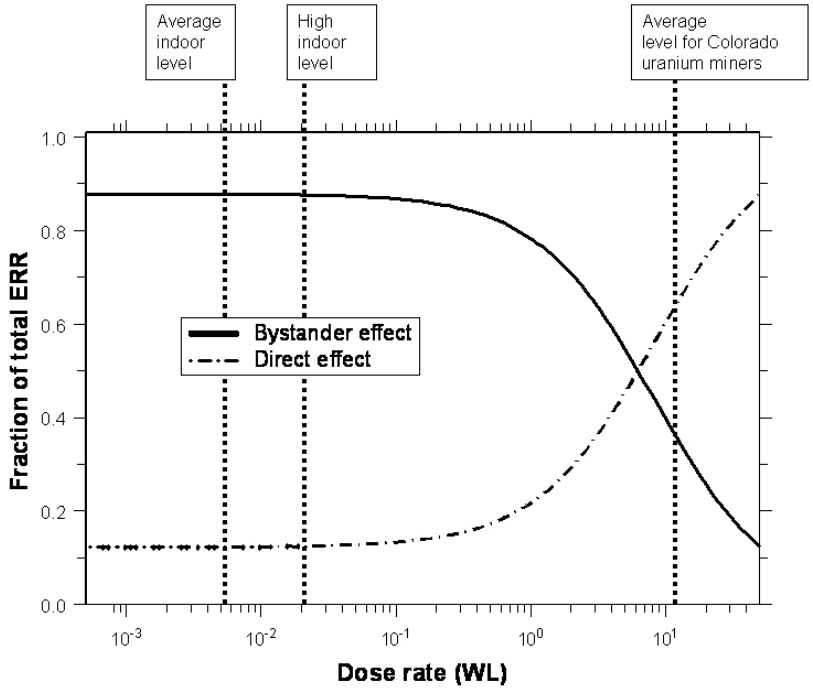

Fig 4. Measured and predicted ERRs at various doses and dose rates. The data points at dose rates >0.04 WL are derived from uranium miners, and those ≤0.04 WL are derived from domestic exposure. The predicted dose responses (lines) correspond to the midpoints of the WL values for each panel (*e.g.,* 0.005 WL in panel A, 0.05 WL in panel B, and so on). In panel I (>15 WL), the prediction is for 20 WL. These dose responses were generated by the initiation-only model (Eq. 9).

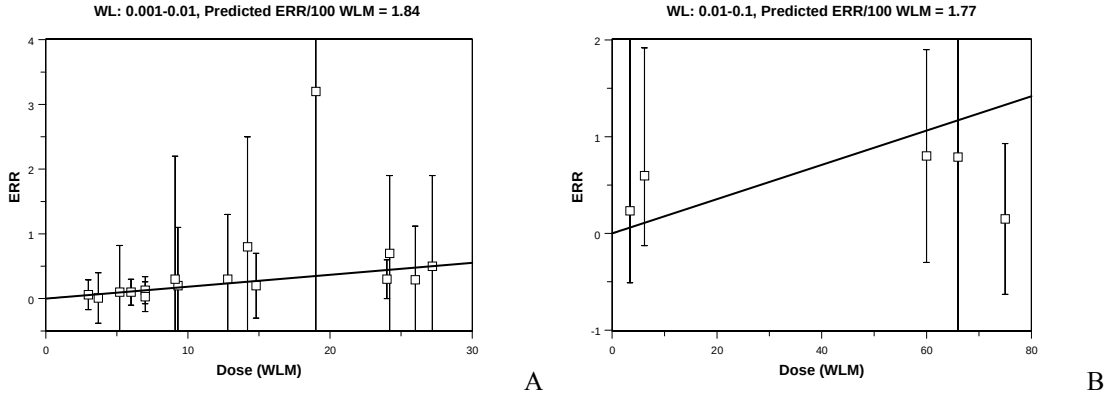

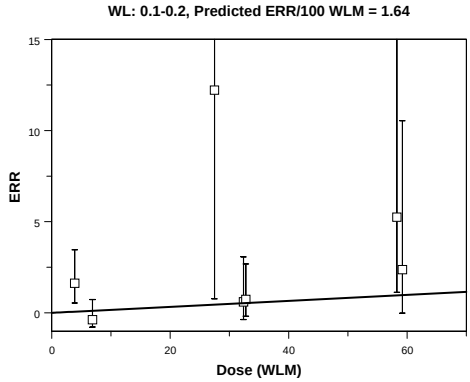
WL: 0.1-0.2, Predicted ERR/100 WLM = 1.64
ERR
Dose (WLM)

C

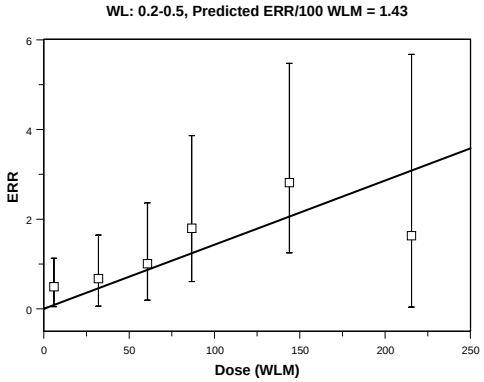
WL: 0.2-0.5, Predicted ERR/100 WLM = 1.43
ERR
Dose (WLM)

D

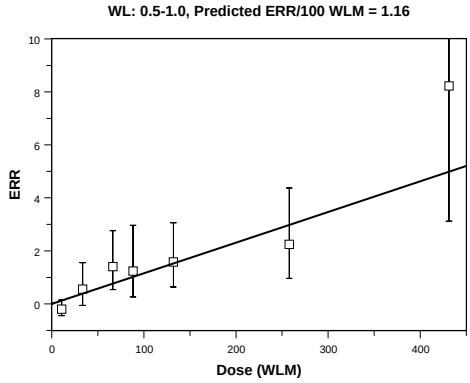
WL: 0.5-1.0, Predicted ERR/100 WLM = 1.16
ERR
Dose (WLM)

E

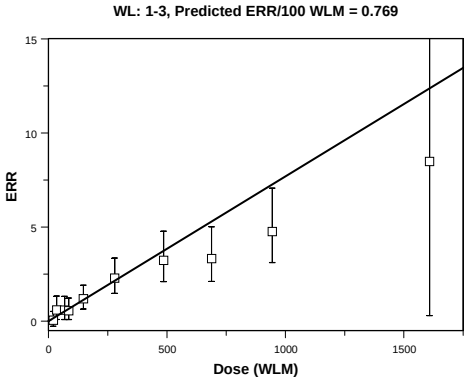
WL: 1-3, Predicted ERR/100 WLM = 0.769
ERR
Dose (WLM)

F

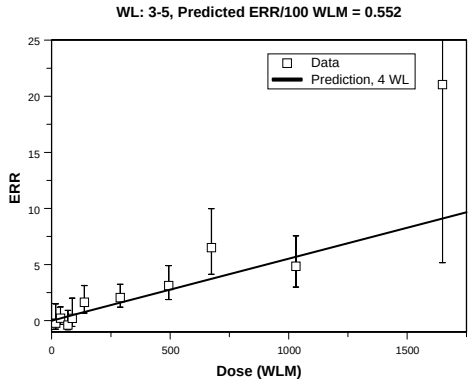
WL: 3-5, Predicted ERR/100 WLM = 0.552
Data
Prediction, 4 WL
ERR
Dose (WLM)

G

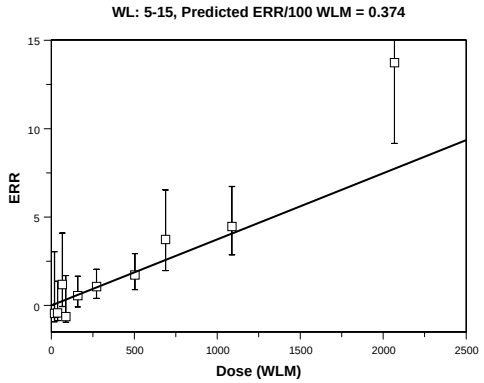
WL: 5-15, Predicted ERR/100 WLM = 0.374
ERR
Dose (WLM)

H

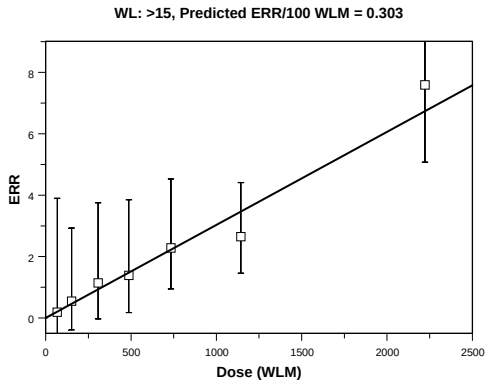
WL: >15, Predicted ERR/100 WLM = 0.303
ERR
Dose (WLM)

I

Fig 5. Measured and predicted ERRs at various doses and dose rates for the PNNL rat data (Wistar strain rats). The error bars were estimated as described in the text by transferring relative risks from the analysis by Heidenreich *et al.* to data from Kaiser *et al.*. To improve visual presentation, some data points were moved laterally in the figure (but not during data fitting), so error bars would not overlap. Fits by both the initiation-only (linear with dose, Eq. 9) and initiation plus promotion (non-linear with dose, Eq. 21) models are shown as dashed and solid lines, respectively. For the initiation-only model, predicted ERR/100 WLM slopes are listed in each panel.

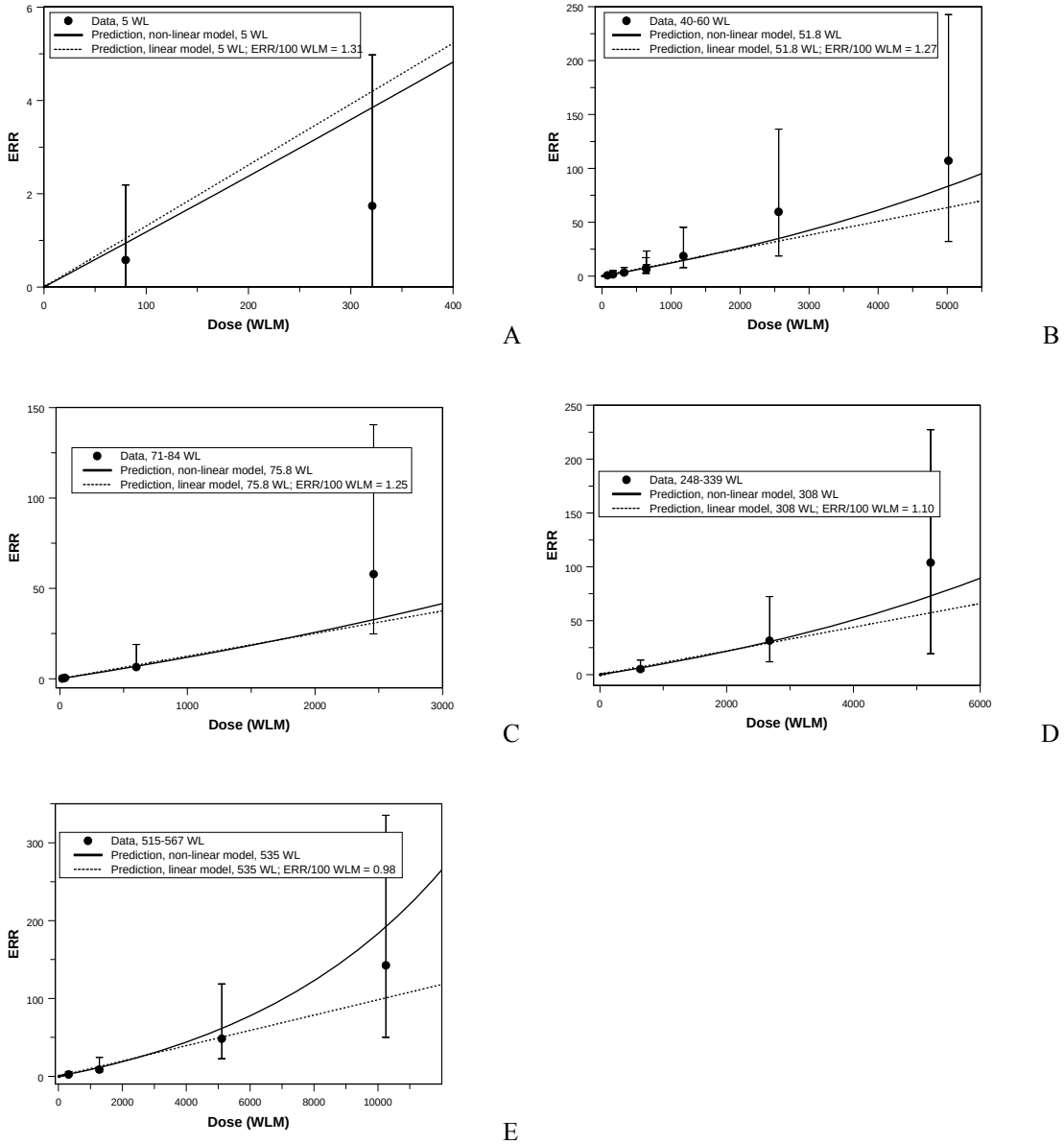

Fig 6. Measured and predicted ERRs at various doses and dose rates for the pooled CEA and AEAT rat data (Sprague-Dawley strain rats). The data points are transcribed from Kaiser *et al.*, without error bars. Fits by both the initiation-only (linear with dose, Eq. 9) and initiation plus promotion (non-linear with dose,

Eq. 21) models are shown as dashed and solid lines, respectively. For the initiation-only model, predicted ERR/100 WLM slopes are listed in each panel.

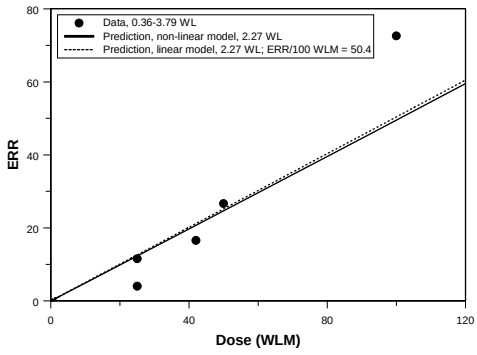

A

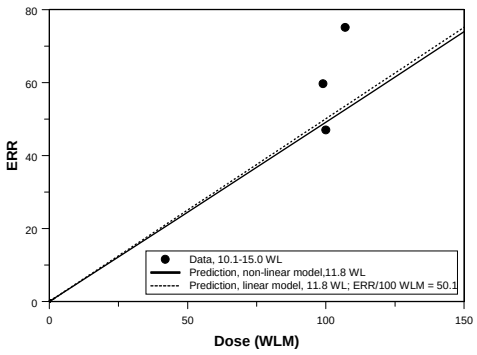

B

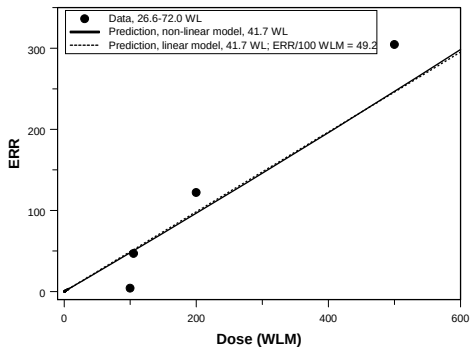

C

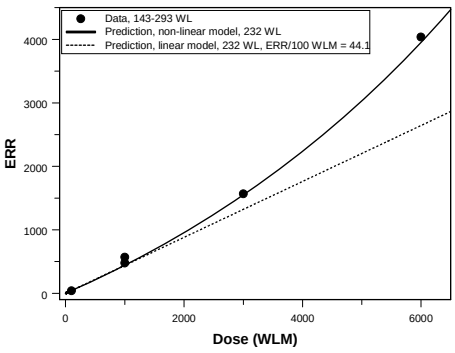

D

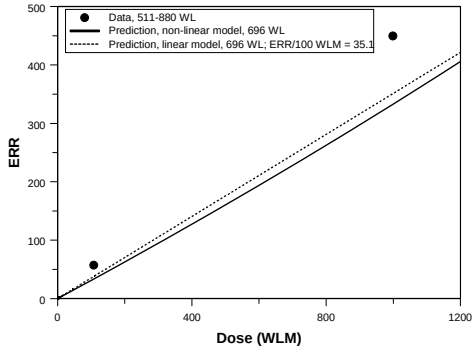

E

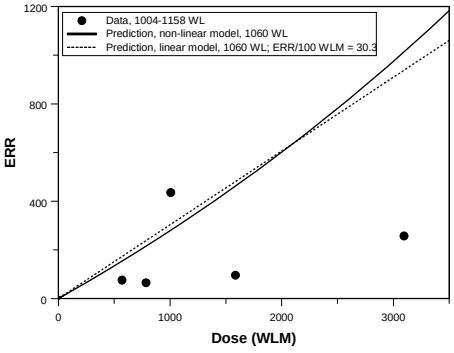

F

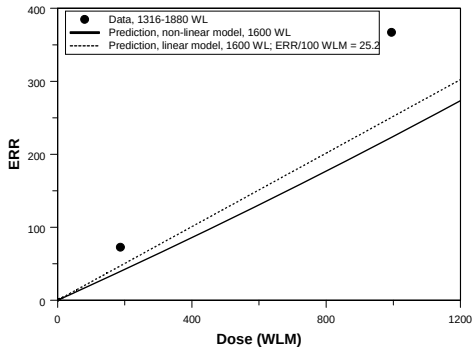

G

Discussion

Previously we presented a mechanistic biophysical model of spatial propagation of the bystander effect in vitro after high-dose, acute, spatially inhomogeneous exposure to high-LET radiation. Here we discuss an extension of the same concepts to a different situation – long-term low dose rate exposure to radon. In both cases, the main assumption is that radiation not only causes cellular damage by direct effects (*i.e.,* traversal of the cell by an ionizing track), but also produces additional indirect damage by activating signaling pathways which induce cells to become stressed. These signals are able to propagate to cells, which have not been directly "hit" by any ionizing tracks, causing the bystander effect.

Our analysis suggests that the bystander effect is the major contributor to radiation-induced ERR at low dose rates (< 1 WL), which are most likely to be encountered by humans in radon-contaminated homes. The bystander effect is also apparently responsible for the inverse dose rate effect (*i.e.,* an increased ERR per unit dose at low dose rates, compared with high dose rates) seen with radon exposure. The magnitude of the inverse dose rate affect is as high as 8-fold, as dose rate varies from zero to infinity. Not taking it into account by directly extrapolating risks from high to low dose rates (*e.g.,* from data on uranium miners at exposure levels of > 1 WL to typical domestic exposure levels of 0.005-0.02 WL) would, therefore, underestimate the hazard substantially. Our model, which incorporates direct and bystander-induced cell initiation, provides a relatively simple analytically solvable formalism for explaining the inverse dose rate effect, and quantifying its magnitude.

The model can provide some insight into details of the bystander effect. For example, it is possible to use the parameter values obtained by fitting the model to human data to estimate the spatial range of bystander signal propagation, and/or the characteristic time needed for cells to stop responding to the signal (*i.e.,* its effective biological decay time). A discussion of this issue is provided in Appendix A.

Throughout the paper, we assumed that radon exposure occurs at a constant dose rate. This is likely to be true for domestic exposure, but is not true for other situations – for example, uranium miners were

exposed to much higher dose rates before mine ventilation techniques were improved in the 1950s, than subsequently (BEIR VI, 1999). A procedure for adapting our model to conditions where the dose rate is piecewise-variable (*e.g.,* initially high, and then low) is provided in Appendix B.

At very high radon doses (> 2500 WLM), which have been investigated only on laboratory animals, the initiation-only model does not describe the data as well, as a promotion plus initiation model. Our simplified explanation for promotion as the byproduct of compensatory proliferation following cell killing by radiation can fit the high-dose data adequately. A better fit to these data would probably require a more complex approach, which considers the dependence of epithelial cell proliferation rates on dose and dose rate. Such an approach is beyond the scope of the current model, involves extra adjustable parameters, and is likely to be of limited practical utility because the very high doses at which it would differ from the current model are unlikely to ever be encountered by humans.

Of course, our hypothesis that the inverse dose rate effect in radon-induced lung carcinogenesis is caused by bystander phenomena needs to be tested experimentally. Our model merely provides a mathematical formalism for calculating the inverse dose rate effect, which is mechanistically plausible, considering the data now available. The formalism contains only three parameters (or four, if promotion is included), and is, consequently, readily testable. In principle, the model can be adapted to situations of low-LET radiation exposure, where inverse dose rate effects (and bystander effects) have sometimes also been observed. We are currently in the process of performing the adaptation, using low-LET data sets.

Appendix A: Estimating the Spatial Range of Bystander Signals

The likely biological picture of the bystander effect suggests that the minimum dose rate at which a substantial fraction of susceptible cells (*e.g.,* ½) can be activated is defined as follows: In each group of cells (C), which are located within the spatial range of bystander signal propagation, at least one cell (or cell nucleus) is traversed by an ionizing track per time T_c, which is the characteristic time needed for an activated cell to return to background state ($T_c = 1/c_3$). This condition can be used to estimate either the number of cells per group (C), which is an indirect measure of signal range, or the characteristic deactivation time T_c.

The number of ionizing traversals per cell per unit of time (N, units: traversals/cell/h) when $R = k$ (so that half of the cells susceptible to the bystander signal are activated at any one time in the steady-state) is given by the following formula:

$$N = k\,A\,B, \qquad \text{Eq. A1}$$

where k is as defined in the main text, A is the number of traversals per cell per unit dose (traversals/cell/WLM), and B is the dose rate conversion factor (WLM/WL/h). The best-fit value of k = 1.007 WL for human data, A = 0.01 traversals/cell/WLM (*2*), and B = 1/170 WLM/WL/h (according to the definitions of WL and WLM). Consequently, $N = 5.924 \times 10^{-5}$ traversals/cell/h.

As defined above, the minimum condition for activating many cells is:

$$N\,C\,T_c = 1 \qquad \text{Eq. A2}$$

Thus, $C = 1/(N\,T_c) = 16882/T$ cells, where T_c is in hours. Thus, the value of k obtained from the human data implies that if reversion from activated to background state happens quickly (*e.g.,* over minutes to hours), then the spatial range of the bystander signal is likely to be large (C is on the order of thousands to tens of thousands of cells). However, if reversion happens more slowly, such as over days to weeks, the signal range should be much smaller, so that only a few adjacent cells can activate each other.

Alternatively, assuming that C is known, one can estimate T_c: $T_c = 1/(N\,C)$. For example, other studies indicate that the bystander signal range can be as large as 1 mm in vitro. Assuming a cell diameter of 30 μm, this range corresponds to about 33 cell diameters. The 3-dimensional volume within which the signal can propagate would then enclose $4/3\pi 33^3 = C = 1.5\square 10^5$ cells. By substitution, the corresponding value of T_c is: $T_c = 0.109$ h = 6.5 minutes. This suggests that either bystander signaling and bystander cell reaction in the lung occurs very rapidly (activation and deactivation occur on the time scale of minutes), or that the signal range estimated in vitro using multiple α-particle traversals per irradiated cell for multiple cells is too large to apply in vivo. The differences may also be due to differences in cell type between in vitro experiments (keratinocytes) and the respiratory system, where radon exposure occurs. For example, if the range in vivo is actually 0.1 mm = 3.3 cells, then a much longer characteristic deactivation time of $T_c = 4.5$ days is obtained.

Appendix B: Calculation of Differences in Predicted ERR Between Situations of Constant Dose Rate Vs. Piecewise-Variable Dose Rate

Experimental rats are typically exposed to radon at well-controlled constant dose rates. In contrast, human uranium miners were exposed to a highly variable dose rate, which peaked during the early period of uranium mining (*e.g.,* 1945-1960), and decreased by several-fold thereafter due to improved mine ventilation (*e.g.,* BEIR VI, 1999). Taking these dose rate fluctuations into consideration can improve ERR estimates, compared with using the average dose rate over the whole exposure period. Analyzing each miner individually is beyond the scope of this paper, but it is possible to estimate by how much the ERR estimate produced by our initiation-only model would change, when the dose rate is assumed to be piecewise-variable, rather than constant. This calculation is presented here:

For a constant dose rate (R), the initiation rate $F_i(R,t)$ as function of radiation dose rate and time (t) is given by Eq. 8 in the text. The ERR is the time integral of $F_i(R,t)$ from time zero until the time when radiation stops (T). Since $F_i(R,t)$ in our initiation-only model does not depend on time, the integral is simply the product of $F_i(R,t)\,T$, which is given by Eq. 9 in the text.

Now we assume that the radiation is administered at piecewise-different dose rates, R_1 and R_2. The conditions are: (1) From time zero until a certain time τ, the dose rate is R_1. The assumption is that $0 < \tau < T$. (2) From time τ until time T, the dose rate is R_2. (3) The average dose rate over time interval T is R, so that $R\,T = D$.

Fig. B1. Diagrammatic representation of radon exposure at piecewise-variable dose rates.

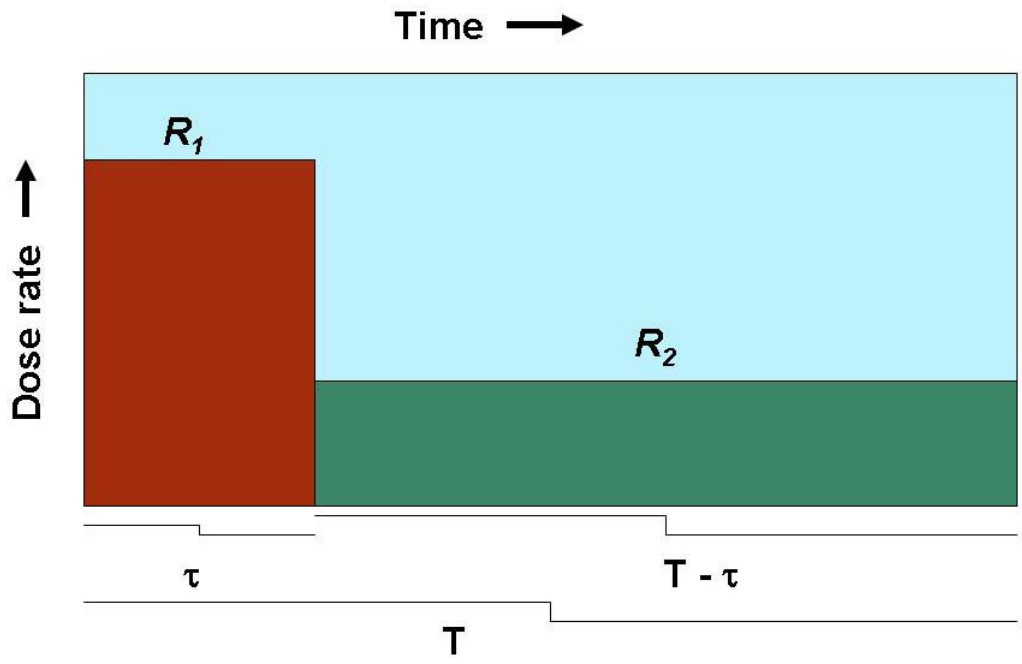

These conditions are schematically shown in Fig. B1. They can be expressed mathematically in the form of the following system of four equations, where m and n are adjustable parameters:

$$\begin{aligned} \tau &= T/n \\ T &= D/R \\ R_1 &= m\,R \\ D &= R_1\,\tau + R_2\,(T-\tau) \end{aligned} \qquad \text{Eq. B1}$$

This system with four unknown variables (τ, T, R_1, R_2) can be solved to express each variable in terms of the known variables R and D. The solutions are:

$$\begin{aligned} \tau &= D/(n\,R) \\ T &= D/R \\ R_1 &= m\,R \\ R_2 &= (R - m\,R/n)\,(1 - 1/n) \end{aligned} \qquad \text{Eq. B2}$$

The expression for ERR for the piecewise dose rates (called ERR_p) is conceptually the same as Eq. 9 in the text, just with two time intervals (τ and $T - \tau$) and two corresponding dose rates (R_1 and R_2):

$$ERR_p = (a\,R_1 + c/(1 + k/R_1))\,\tau + (a\,R_2 + c/(1 + k/R_2))\,(T - \tau) \qquad \text{Eq. B3}$$

Substituting Eq. B2 into Eq. B3 and simplifying, one gets the following solution for ERR_p in terms of R and D:

$$\begin{aligned} ERR_p = D\,[&a\,m\,(m-n)\,R^2 + [-a\,n\,((1+m) - 2\,m)\,k + m\,c\,(m-n)]\,R \\ &- k\,(n-1)\,(a\,k + c)]/\,[(R\,(m-n) + k\,(1-n))\,(m\,R + k)] \end{aligned} \qquad \text{Eq. B4}$$

To compare the risk of a piecewise dose rate situation with that of a constant dose rate situation, one can define the risk ratio (X) as the ratio of Eq. B4 to Eq. 9:

$$X = ERR_p/ERR \qquad \text{Eq. B5}$$

The ratio X does not depend on dose (D cancels out), but does depend on dose rate (R). The behavior of X using best-fit parameters for the human uranium miner and domestic exposure data ($a = 2.253 \times 10^{-3}$ WLM^{-1}, $c = 1.635 \times 10^{-2}$ WLM/WL, $k = 1.007$ WL), and an extreme case of uneven dose rate ($n = 5$ and $m = 5$, *i.e.,* $\tau = T/5$ and $R_1 = 5\ R$) is shown in Fig. B2.

Fig. B2 indicates that under these relatively extreme assumptions about uneven dose rate (5-fold difference between the initial dose rate and the average dose rate), the maximum difference in ERR is about 2-fold for the uneven dose rate scenario versus the constant average dose rate scenario. For other, less extreme, situations, the ERR difference is smaller (*i.e., X* is closer to unity). The implication of these results is that predictions of our initiation-only model are not overly sensitive to fluctuations in dose rate. Some examples are provided in Table B1.

Fig. B2. Dependence of the risk ratio (X) for radon exposure at piecewise-variable dose rates to exposure at constant dose rate on average dose rate (R). The parameters used are discussed in the text.

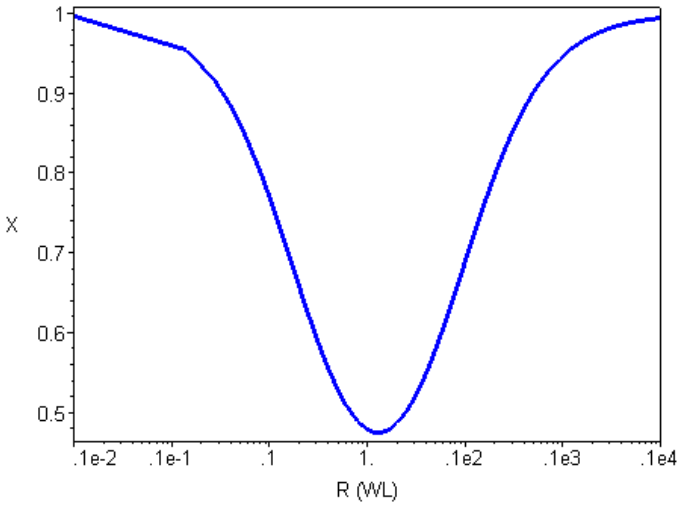

Table B1. Dependence of the minimum risk ratio (min(X)) for radon exposure at piecewise-variable dose rates to exposure at constant dose rate, as parameters m and n are varied. In each case, a solution can only be obtained as long as $m \leq n$.

n $1/n$ = fraction of time spent at first dose rate, R_1	m = factor by which the first dose rate (R_1) is higher than the average dose rate (R)	min(X) = minimum ratio of ERR_p/ERR
5	5	0.474
	3	0.865
	2	0.961
3	3	0.594
	2	0.912
	1.5	0.977
2	2	0.718
	1.5	0.948
	1.2	0.992
1.5	1.5	0.823
	1.2	0.982
	1.1	0.996

References

Biophysical models of radiation bystander effects: 1. Spatial effects in three-dimensional tissues. Radiat Res. 2007 Dec;168(6):741-9.

Shuryak I, Sachs RK, Brenner DJ. Biophysical models of radiation bystander effects: 2. The relationship between the inverse dose rate effect and the bystander effect. In preparation

Shuryak I, Hahnfeldt P, Hlatky L, Sachs RK, Brenner DJ. A new view of radiation-induced cancer: integrating short- and long-term processes. Part I: Approach. Radiat Environ Biophys. 2009 Jun 18. [Epub ahead of print]